ACS OMEGA
Article
Cite This: ACS Omega 2018, 3, 5141−5154

Tailoring Hydrophobic Interactions between Probes and Amyloid-β Peptides for Fluorescent Monitoring of Amyloid-β Aggregation

Sonam Kim,[†,⊥] Hyuck Jin Lee,[‡,⊥,#] Eunju Nam,[§,⊥,#] Donghyun Jeong,[∥] Jaeheung Cho,[*,∥] Mi Hee Lim,[*,‡,#] and Youngmin You[*,†]

[†]Division of Chemical Engineering and Materials Science, Ewha Womans University, Seoul 03760, Republic of Korea
[‡]Department of Chemistry, Korea Advanced Institute of Science and Technology (KAIST), Daejeon 34141, Republic of Korea
[§]Department of Chemistry, Ulsan National Institute of Science and Technology (UNIST), Ulsan 44919, Republic of Korea
[∥]Department of Emerging Materials Science, Daegu Gyeongbuk Institute of Science and Technology (DGIST), Daegu 42988, Republic of Korea

Supporting Information

ABSTRACT: Despite their unique advantages, the full potential of molecular probes for fluorescent monitoring of amyloid-β (Aβ) aggregates has not been fully exploited. This limited utility stems from the lack of knowledge about the hydrophobic interactions between the molecules of Aβ probes, as well as those between the probe and the Aβ aggregate. Herein, we report the first mechanistic study, which firmly establishes a structure−signaling relationship of fluorescent Aβ probes. We synthesized a series of five fluorescent Aβ probes based on an archetypal donor−acceptor−donor scaffold (denoted as **SN1−SN5**). The arylamino donor moieties were systematically varied to identify molecular factors that could influence the interactions between molecules of each probe and that could influence their fluorescence outcomes in conditions mimicking the biological milieu. Our probes displayed different responses to aggregates of Aβ, Aβ_{40} and Aβ_{42}, two major isoforms found in Alzheimer's disease: **SN2**, having pyrrolidine donors, showed noticeable ratiometric fluorescence responses ($\Delta\nu$ = 797 cm^{-1}) to the Aβ_{40} and Aβ_{42} samples that contained oligomeric species, whereas **SN4**, having *N*-methylpiperazine donors, produced significant fluorescence turn-on signaling in response to Aβ aggregates, including oligomers, protofibrils, and fibrils (with turn-on ratios of 14 and 10 for Aβ_{42} and Aβ_{40}, respectively). Mechanistic investigations were carried out by performing field-emission scanning electron microscopy, X-ray crystallography, UV−vis absorption spectroscopy, and steady-state and transient photoluminescence spectroscopy experiments. The studies revealed that the **SN** probes underwent preassembly prior to interacting with the Aβ species and that the preassembled structures depended profoundly on the subtle differences between the amino moieties of the different probes. Importantly, the studies demonstrated that the mode of fluorescence signaling (i.e., ratiometric response versus turn-on response) was primarily governed by stacking geometries within the probe preassemblies. Specifically, ratiometric fluorescence responses were observed for probes capable of forming J-assembly, whereas fluorescence turn-on responses were obtained for probes incapable of forming J-aggregates. This finding provides an important guideline to follow in future efforts at developing fluorescent probes for Aβ aggregation. We also conclude, on the basis of our study, that the rational design of such fluorescent probes should consider interactions between the probe molecules, as well as those between Aβ peptides and the probe molecule.

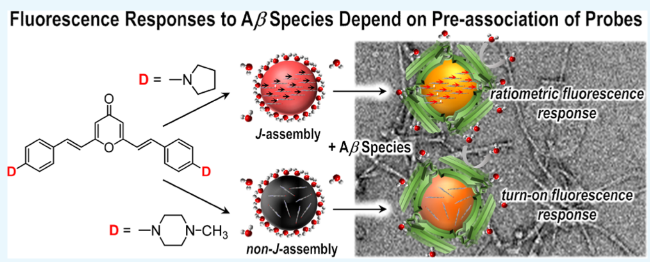

■ INTRODUCTION

Amyloid-β (Aβ) aggregates are assembled superstructures of misfolded Aβ peptides.[1,2] The genesis and progress of Aβ aggregation are characterized by dynamic changes in the heterogenic population of different forms of Aβ, including monomers, low- and high-molecular-weight oligomers, protofibrils, and fibrils.[3−9] A growing amount of evidence has indicated that different individual species of Aβ aggregates have different effects on the pathology of Alzheimer's diseases (AD).[8,10−19] To understand the detailed role of Aβ aggregates in AD pathogenesis, chemical tools capable of detecting Aβ aggregation have been developed and employed.[20−28]

Among the available chemical tools, fluorescent probes are the most suitable for monitoring Aβ species with respect to sensitivity, dynamic ranges, and ability for real-time imaging. Various fluorescent probes have been designed on the basis of the structures of traditional stains for Aβ fibrils, such as thioflavin-T (ThT).[2,29,30] Several molecular strategies have been employed to shift emission wavelengths bathochromically, with these strategies having included extending π-conjugated back-

Received: February 18, 2018
Accepted: April 23, 2018
Published: May 11, 2018

   DOI: 10.1021/acsomega.8b00286
ACS Omega 2018, 3, 5141−5154

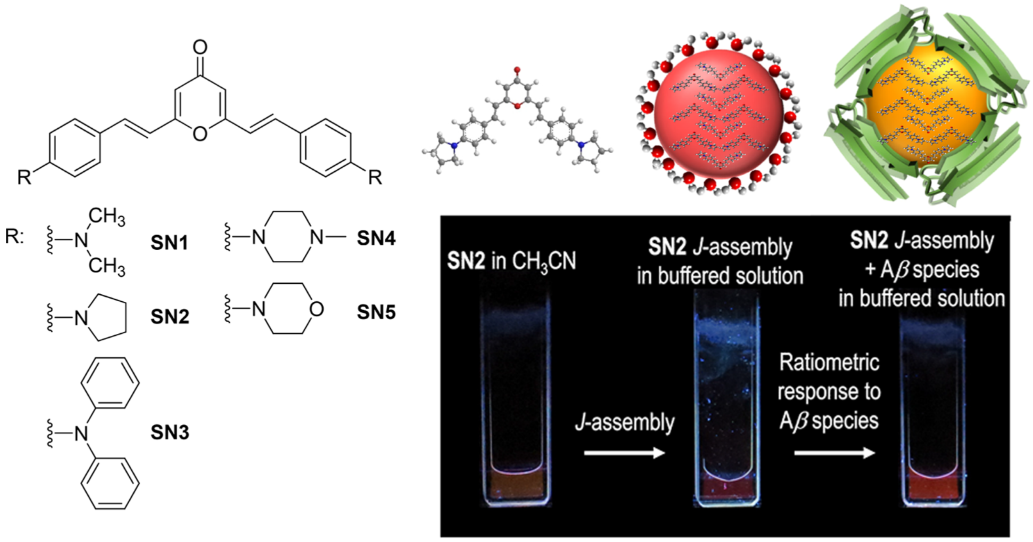

Figure 1. Chemical structures of the **SN** compounds and fluorescence responses of **SN2** under different conditions, including the presence of Aβ peptides.

Table 1. Photophysical Data for the SN Compounds[a]

	λ_{abs} (nm; log ε)	λ_{ems} (nm)[b]	Φ_f[c]	τ_{obs} (ns)[d]	k_r (10^7 s^{-1})[e]	k_{nr} (10^7 s^{-1})[f]	clog P[g]
SN1	417 (4.43)	559	0.006	0.21	2.9	485	2.61
SN2	423 (4.26)	559	0.011	0.31	3.6	321	1.34
SN3	409 (4.61)	562	0.018	0.56	3.2	177	2.08
SN4	404 (4.50)	565	0.004	0.49	0.82	204	1.20
SN5	396 (4.38)	557	0.005	0.40	1.3	250	0.73

[a]10 μM in CH_3CN, 298 K. [b]Excitation wavelengths: **SN1**, 417 nm; **SN2**, 399 nm; **SN3**, 409 nm; **SN4**, 404 nm; and **SN5**, 396 nm. [c]Fluorescence quantum yield relative to that of a 9,10-diphenylanthracene standard (toluene, $\Phi_f = 1.00$).[73] [d]Fluorescence lifetime obtained after picosecond pulsed laser photoexcitation at 377 nm (temporal resolution = 8 ps; fluorescence signals were monitored at the peak wavelengths of the fluorescence emission). [e]Radiative rate constant. [f]Nonradiative rate constant. [g]Partition coefficient determined in *n*-octanol and a buffered aqueous solution (10 mM phosphate-buffered saline (PBS), pH 7.4): clog $P = \log(C_o/C_w)$, where C_0 and C_w are the concentrations of the **SN** compound partitioned into *n*-octanol and the PBS buffer, respectively.

bones,[31−38] and introducing an electron donor (D) and an electron acceptor (A) at each terminus of a π-conjugated framework.[24,39−70] These designs entailed enhancing the lipophilicity of probes, which could be beneficial for increasing their affinity for hydrophobic Aβ aggregates and their ability to cross the blood−brain barrier.[41,53]

Increasing the lipophilicity of a probe may, however, result in the spontaneous aggregation of the probe molecules in aqueous media. Actually, this cohesion is unavoidable for the majority of fluorescent probes because they are based on rigid, planar π-scaffolds, such as polyenes or fused aromatics.[26−28] The self-association of probe molecules makes it difficult to predict and to interpret the fluorescence response to Aβ aggregates, posing significant challenges in the rational design of Aβ probes. This notion is supported by previous observations with the enhancement or quenching of fluorescence emission attributed to subtle differences between the structures of the self-associated and monomeric probe molecules.[71,72] Note that previous research has mainly focused on binding interactions of probe molecules with hydrophobic clefts of Aβ proteins but has mostly ignored the multitude of other intermolecular interactions present in various ensembles of probes and Aβ peptides. The resulting limited knowledge has impeded the exploitation of the full potential of fluorescent probes for monitoring Aβ aggregation.

Herein, we report the association and Aβ detection properties of a novel series of D−A−D fluorophores, denoted as **SN1**−**SN5**, with demonstration of molecular level mechanisms for their fluorescence responses to Aβ aggregation. The fluorophores consisted of *p*-(*N*,*N*-disubstituted amino)styryl donors and a pyrone acceptor (Figure 1). Fluorescence responses of the **SN** compounds to aggregation processes of two major isoforms of Aβ, Aβ_{40} and Aβ_{42},[5] were monitored. By carrying out photophysical and X-ray crystallographic experiments, we found **SN1** and **SN2** to spontaneously organize into slipped J-stacks in buffered aqueous solutions. Further mechanistic studies of these fluorophores, including studies involving steady-state and transient photophysical measurements, were performed to elucidate the molecular origin of their fluorescence responses to Aβ aggregates.

■ RESULTS AND DISCUSSION

Synthesis and Fluorescence Studies of the Molecular Probes for Aβ Aggregation. The molecular constructs of the **SN** compounds were based on a bent D−A−D scaffold. This design was chosen because the presence of a permanent dipole moment in such a scaffold can bolster molecular stacking. Five **SN** compounds (**SN1**−**SN5**) were prepared, each through a condensation reaction between pyrone and a *p*-aminobenzaldehyde in the presence of sodium ethoxide. Structures of the *p*-amino entities were varied and included *N*,*N*-dimethylamine (**SN1**), pyrrolidine (**SN2**), *N*,*N*-diphenylamine (**SN3**), *N*-methylpiperazine (**SN4**), and morpholine (**SN5**). Synthetic

DOI: 10.1021/acsomega.8b00286
ACS Omega 2018, 3, 5141−5154

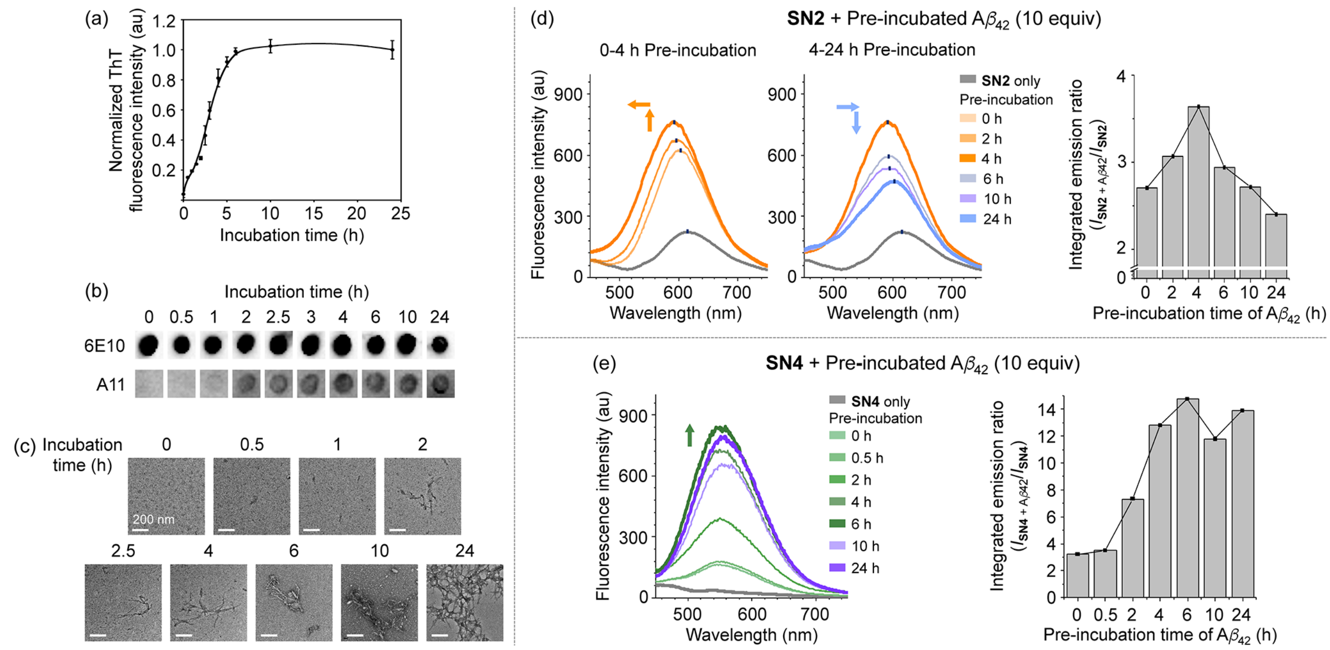

Figure 2. Fluorescence responses of **SN2** and **SN4** to Aβ_{42} aggregation. The extend of which β-sheet-rich Aβ_{42} aggregates formed was monitored using (a) the ThT assay, (b) the dot blot assay, and (c) TEM. Conditions: [Aβ_{42}] = 20 μM; pH 7.4; 37 °C; constant agitation. The normalized intensities of the dot blots are presented in SI, Figure S13. Fluorescence spectra taken for (d) **SN2** and (e) **SN4** upon being treated for 10 min with the Aβ_{42} species (10 equiv), generated by preincubation for various durations (0−24 h; left), and the ratios of the integrated emission intensities of the **SN** probes in the presence over absence of Aβ_{42} aggregates (right). Conditions: [Aβ_{42}] = 20 μM; [**SN2** or **SN4**] = 2 μM; pH 7.4; λ_{ex} = 399 and 404 nm for **SN2** and **SN4**, respectively.

details and spectroscopic identification data of the **SN** compounds are summarized in the Supporting Information (SI, Figures S1−S10). The **SN** compounds displayed yellow to orange fluorescence when dissolved in organic solutions. For instance, **SN2** was observed to be moderately fluorescent in CH_3CN, with an emission peak wavelength (λ_{em}) of 559 nm and a fluorescence quantum yield (Φ_f) of 0.011. Photophysical data for the **SN** compounds are compiled in Table 1.

The ability to use the **SN** compounds for fluorescence monitoring of Aβ aggregation was investigated by employing Aβ_{42} and Aβ_{40}, two major Aβ isoforms found in the AD-affected brain (Figures 2 and 3, and SI, Figures S11−S13).[5,7,74] The generation of both Aβ_{42} and Aβ_{40} aggregates was tracked using the ThT assay, dot blot assay, and transmission electron microscopy (TEM, Figures 2a−c and 3a−c). In the case of Aβ_{42}, a rapid onset of the elongation phase of aggregation occurred (Figure 2a), whereas the aggregation of Aβ_{40} exhibited a slightly longer lag phase (Figure 3a). In addition, the dot blot assay using two different anti-Aβ antibodies (i.e., 6E10 for Aβ species[7,75] and A11 for structured oligomers[76]) indicated the formation of A11-detectable structured oligomers after 2 and 1.5 h incubation of Aβ_{42} and Aβ_{40}, respectively (Figures 2b and 3b). The morphologies of Aβ aggregates obtained from different incubation time points were also monitored through TEM (Figures 2c and 3c). Fibrilization of both Aβ_{42} and Aβ_{40} was identified at longer incubation time (10 and 24 h). The distinct aggregation characteristics of Aβ_{42} and Aβ_{40} observed through three different methods were consistent with the results reported previously.[5,13,77,78] Note that we applied the Aβ species generated upon aggregation to our probes because the isolation of specific Aβ species is difficult due to multiple aggregation pathways and sensitivity on experimental conditions for forming Aβ aggregates.[8]

We measured the fluorescence responses of **SN1**−**SN5** to the aggregation of Aβ_{42} and Aβ_{40} (10 equiv). The fluorescence spectra of both **SN2** and **SN4** were observed to be considerably affected by the progress of Aβ aggregation (Figures 2d,e and 3d,e), whereas **SN1**, **SN3**, and **SN5** did not produce such responses (SI, Figure S11). When Aβ aggregates were treated with **SN2** and **SN4** followed by being imaged using a confocal microscope, noticeable fluorescence signals were observed, indicative of the interaction between Aβ aggregates and our probes (SI, Figure S12). In particular, ratiometric fluorescence monitoring of Aβ aggregation was found to be possible when using **SN2** as the fluorescence probe: (i) **SN2** yielded a hypsochromic shift (λ_{em} = 618 → 588 nm), along with a 3.6-fold enhancement in the fluorescence intensity, upon interacting with Aβ_{42} species that were pre-incubated for 4 h (Figure 2d, left); and (ii) the fluorescence intensity decreased with a small bathochromic shift (λ_{em} = 588 → 600 nm), when **SN2** was treated with Aβ_{42} species preincubated for 6, 10, and 24 h (Figure 2d, middle). Similar ratiometric fluorescence responses to Aβ_{40} were also observed. As depicted in Figure 3d, **SN2** showed the most enhanced (2.6-fold) and blue-shifted (λ_{em} = 618 → 589 nm) fluorescence emission in the presence of the Aβ_{40} species preincubated for 5 h. In contrast, fluorescence turn-off responses with a bathochromic shift (λ_{em} = 589 → 600 nm) were observed in the presence of Aβ_{40} aggregates generated by longer durations of incubation (i.e., 24 h). For both Aβ_{42} and Aβ_{40}, the turn-on ratiometric fluorescence responses of **SN2** were found to be more discernible when treated with the Aβ samples that contained oligomeric aggregates than those mainly having monomers and fibrils (Figures 2d and 3d). Such specificity for oligomers could have resulted from greater hydrophobic interactions, because, compared to mature fibrils, oligomeric species have been suggested to have more exposed hydrophobic

DOI: 10.1021/acsomega.8b00286
ACS Omega 2018, 3, 5141−5154

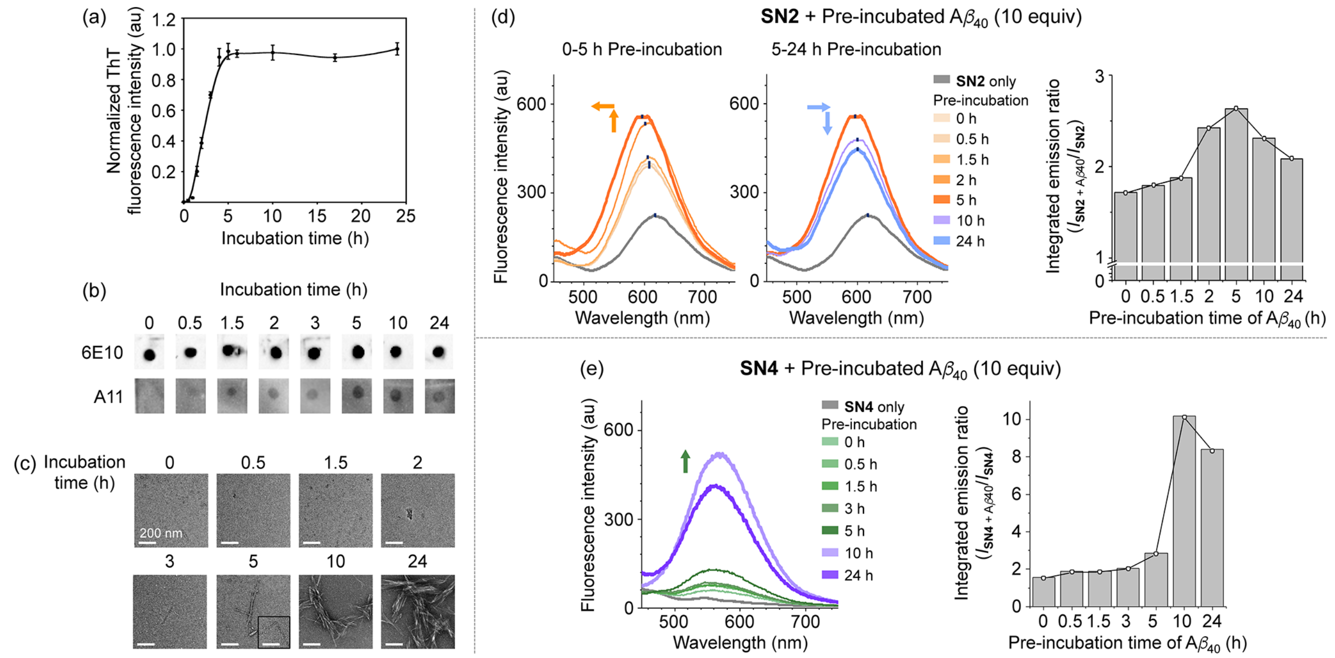

Figure 3. Fluorescence responses of **SN2** and **SN4** to Aβ_{40} aggregation. The generation of β-sheet-rich Aβ_{40} aggregates was detected using (a) the ThT assay, (b) the dot blot assay, and (c) TEM. Conditions: [Aβ_{40}] = 20 μM; pH 7.4; 37 °C; constant agitation. The normalized intensities of the dot blots are presented in SI, Figure S13. Fluorescence spectra of (d) **SN2** and (e) **SN4** after being treated for 10 min with the Aβ_{40} species (10 equiv), formed by preincubation for various durations (0−24 h; left), and the ratios of the integrated emission intensities of the **SN** probes in the presence over absence of Aβ_{40} aggregates (right). Conditions: [Aβ_{40}] = 20 μM; [**SN2** or **SN4**] = 2 μM; pH 7.4; λ_{ex} = 399 and 404 nm for **SN2** and **SN4**, respectively.

groups.[79−82] The detailed mechanisms of the fluorescence responses are discussed in the following section (vide infra).

In the case of **SN4**, fluorescence turn-on responses were observed upon interactions of this probe with Aβ_{42} and Aβ_{40} species. As shown in Figures 2e and 3e, the fluorescence responses of **SN4** were characterized by monotonic increases in intensities in proportion to the preincubation time of the Aβ peptide. Maximum turn-on ratios for Aβ_{42} and Aβ_{40} were measured to be 14 and 10, respectively, and the responses were devoid of noticeable chromic shifts. **SN4** preferentially interacted with Aβ aggregates (e.g., larger Aβ aggregates, including protofibrils and fibrils, especially for Aβ_{40}) over Aβ monomers. Note that the fluorescence responses of both **SN2** and **SN4** to Aβ_{42} were observed to be distinct from those to Aβ_{40}. Compared to Aβ_{40}, Aβ_{42} was found to elicit a greater change in fluorescence at shorter preincubation times. Such specificity could have resulted from the different structural and aggregation properties of Aβ_{42} relative to Aβ_{40}: Aβ_{42} tends to aggregate faster than Aβ_{40}, producing a diverse range of oligomers, including dodecamers.[5,77,78]

Furthermore, **SN2** and **SN4** produced no noticeable response to ubiquitin, a competing protein, whereas **SN1**, **SN3**, and **SN5** did slightly respond to ubiquitin (SI, Figure S14). Both **SN2** and **SN4** could detect Aβ species in a mixture of Aβ aggregates (20 μM) and ubiquitin (20 μM; SI, Figure S15). Moreover, when **SN2** and **SN4** were added to the solutions containing 5 and 10 h preincubated Aβ aggregates and neuro-2a neuroblastoma (N2a) APPwt cell lysates that included various proteins, both compounds presented their fluorescent responses to Aβ species (SI, Figure S15). Taken together, the fluorescence experiments with Aβ demonstrated the feasibility of using **SN2** and **SN4** to monitor Aβ aggregation. The fluorescent responses to the Aβ species depended distinctively on the molecular structures of the probes; **SN2** showed ratiometric fluorescence changes, whereas **SN4** produced fluorescence turn-on responses. Moreover, both **SN2** and **SN4** (2 μM) were not shown to be toxic in living cells for a short incubation time (i.e., 1 h); however, with longer incubation (24 h), **SN4** noticeably indicated cytotoxicity (SI, Figure S16).

Molecular Origin for the Fluorescence Responses to Aβ Aggregation. We hypothesized the contrasting responses of the **SN** probes to Aβ aggregates to be due to different preassociation structures formed by the probes. To validate this hypothesis, we investigated the photophysical properties of all of the **SN** compounds in aqueous solutions. As shown in Figure 4, an enhancement in fluorescence was observed for **SN2** upon the addition of H_2O into the CH_3CN solution. Dynamic light scattering (DLS) and field-emission scanning electron microscopy (FESEM) experiments revealed the formation of globular nanoparticles of **SN2** (Figure 4a,b). The nanoparticle suspension was found to be very stable, as neither particle agglomeration nor precipitation was observed within 3 days of preparation. An enhancement in Φ_f by 1 order of magnitude was observed upon nanoparticle formation (Φ_f = 0.12 in 1:19 v/v CH_3CN/H_2O; λ_{em} = 599 nm; Table 2). This increase was accompanied by a nearly 1 order of magnitude increase in the fluorescence lifetime (τ_{obs}) of **SN2**, from 0.31 ns (CH_3CN) to 1.1 ns (1:19 v/v CH_3CN/H_2O), and by an increase and a decrease, respectively, of the corresponding radiative rate constant (k_r, $k_r = \Phi_f/\tau_{obs}$) and nonradiative rate constant (k_{nr}, $k_{nr} = (1 - \Phi_f)/\tau_{obs}$; k_r, 3.6×10^7 to 1.1×10^8 s^{-1}; k_{nr}, 3.21×10^9 to 8.0×10^8 s^{-1}; Tables 1 and 2). The results suggested that the fluorescence enhancement was due to the system operating under both radiative and nonradiative control. Upon forming nanoparticles, **SN2** showed bathochromic shifts in its UV−vis absorption (by 2560 cm^{-1}) and fluorescence (by 1190 cm^{-1}; Figures 4d,e). These spectroscopic signatures were indicative of J-assembly formation, which involved slipped unidirectional arrangement of

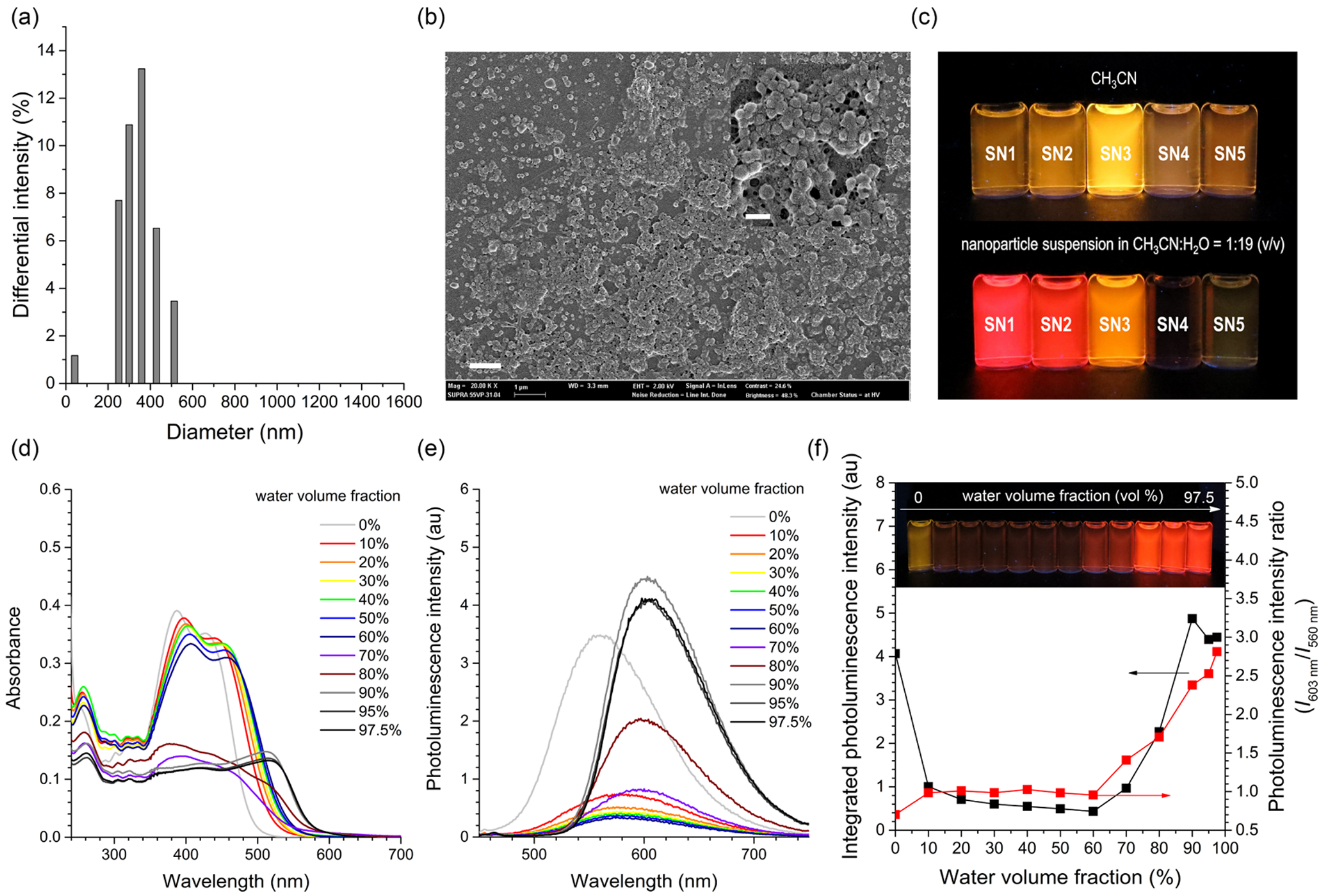

Figure 4. Fluorescent J-assemblies of **SN2**. (a) Distribution of the diameters of **SN2** nanoparticles, determined using DLS. (b) FESEM image of the **SN2** nanoparticles. Scale bar = 1 μm. Inset image is a magnified view. Scale bar = 200 nm. (c) Photograph showing fluorescence emission of the CH_3CN solutions (top) and nanoparticle suspension in CH_3CN/H_2O (1:19, v/v; bottom) of the **SN** compounds subjected to photoirradiation at a wavelength of 365 nm. (d) UV−vis absorption spectra of **SN2** (10 μM; CH_3CN) obtained using various fractions of H_2O (0−97.5%, v/v). (e) Fluorescence spectra of **SN2** (10 μM; CH_3CN) obtained using various fractions of H_2O (0−97.5%, v/v). (f) Changes in the integrated photoluminescence intensity (black) and the photoluminescence intensity ratio (red, $I_{603\ nm}/I_{560\ nm}$) of **SN2** as a function of the added water volume fraction. The inset photograph shows the fluorescence emission of **SN2** in aqueous CH_3CN solutions.

SN2 (vide infra). J-assemblies are beneficial for luminescence applications as they exhibit strong fluorescence emission due to high allowance for radiative transition.[71] Such J-emission was retained in an aqueous solution buffered at pH 7.4 (25 mM piperazine-*N*,*N*′-bis(2-ethanesulfonic acid) (PIPES), 100 mM KCl), demonstrating that the amphiphilic buffer molecules (i.e., PIPES) did not interfere with the **SN2** assembly (SI, Figure S17).

The J-assembly depended on subtle differences in the structures of the amino entities in the **SN** compounds: **SN1** was found to display J-fluorescence emission similar to that of **SN2**, whereas the other tested molecules (i.e., **SN3**, **SN4**, and **SN5**) did not produce such behaviors (see Figure 4c). The UV−vis absorption and fluorescence spectral measurements revealed the presence of a J-transition in the **SN1** nanoparticles, whereas such a behavior was absent for **SN3**, **SN4**, and **SN5** (SI, Figure S18). The inability of **SN3** to participate in J-assembly formation was likely due to increased steric hindrance by *N*,*N*-diphenylamino groups, and the inability for **SN4** and **SN5** was ascribed to the presence of additional basic atoms. On the basis of the results taken together, the **SN** compounds are classified into two groups: (i) those forming highly fluorescent J-assembly, i.e., **SN1** and **SN2**; and (ii) those not forming J-assembly, i.e., **SN3**, **SN4**, and **SN5**. The photophysical parameters of the aggregates of the **SN** compounds are summarized in Table 2.

Table 2. Photophysical Data for the SN Aggregates[a]

	λ_{abs} (nm; log ε)	λ_{ems} (nm)[b]	Φ_f[c]	τ_{obs} (ns)[d]	k_r (10^7 s^{-1})[e]	k_{nr} (10^7 s^{-1})[f]
SN1	535 (4.15)	602	0.11	1.4	7.8	64
SN2	511 (3.89)	599	0.12	1.1	11	80
SN3	413 (4.34)	565	0.048	2.2	2.2	43
SN4	401 (4.28)	572	0.0005	0.40	0.13	250
SN5	376 (3.59)	557	0.004	1.1	3.6	91

[a]Nanoparticle suspension (10 μM) in 1:19 v/v CH_3CN/H_2O, 298 K. [b]Excitation wavelengths: **SN1**, 417 nm; **SN2**, 399 nm; **SN3**, 409 nm; **SN4**, 404 nm; and **SN5**, 396 nm. [c]Fluorescence quantum yield relative to that of a 9,10-diphenylanthracene standard (toluene, Φ_f = 1.00).[73] [d]Fluorescence lifetime obtained after picosecond pulsed laser photoexcitation at a wavelength of 377 nm (temporal resolution = 8 ps; fluorescence signals were monitored at the peak wavelengths of the fluorescence emission). [e]Radiative rate constant. [f]Nonradiative rate constant.

To investigate the structural origin of the J-fluorescence of **SN1** and **SN2**, we obtained single crystals of **SN1**. Several attempts to grow the crystals of **SN2** suitable for X-ray crystallographic analysis were unsuccessful. As shown in Figure 5a, **SN1** adopts a near planar structure having distortion angles between the pyrone core and two phenyl rings to be 8.00 and

DOI: 10.1021/acsomega.8b00286
ACS Omega 2018, 3, 5141−5154

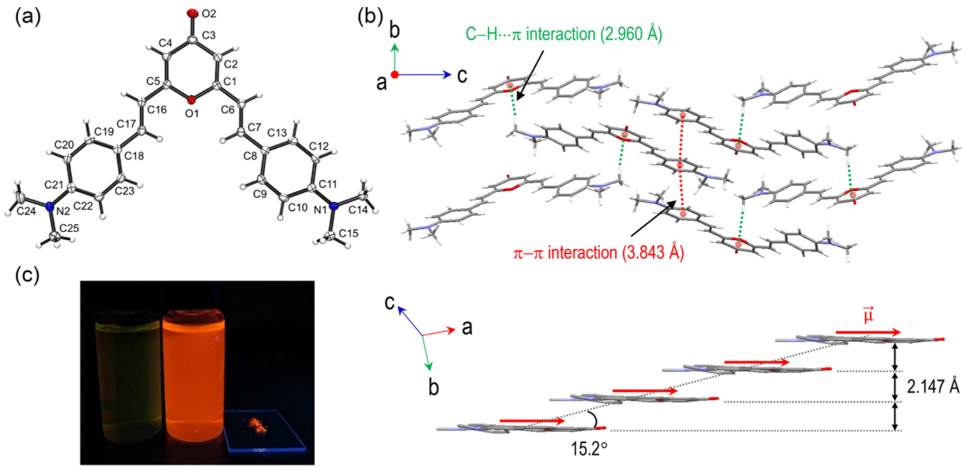

Figure 5. X-ray crystal structure of **SN1**. (a) Oak Ridge thermal ellipsoid plot drawing at 30% probability. (b) Molecular stacking structure. The orange and green dotted lines indicate the intermolecular $\pi-\pi$ (3.843 Å) and C−H···π (2.960 Å) interactions, respectively. The bottom image shows a J-type stack of **SN1** molecules. The red arrows are transition dipole moments. (c) Fluorescence emission of **SN1** obtained under photoexcitation at a wavelength of 365 nm: left, 10 μM **SN1** in CH_3CN; middle, 10 μM **SN1** nanoparticle suspension in CH_3CN/H_2O (1:9, v/v); right, **SN1** single crystals.

3.72°. The molecular stacking structure reveals the presence of short intermolecular contacts of 2.960 and 3.843 Å, which correspond to C−H···π and $\pi-\pi$ interactions, respectively. Geometric parameters for the crystal of **SN1** are piled in SI, Tables S1 and S2. The overall stacking geometry of **SN1** was characterized by a zigzag alignment, where dipolar interactions between the two *p*-(*N*,*N*-dimethylamino)styrylpyrone entities provided a key driving force. In this molecular arrangement, transition dipole moments were calculated using the time-dependent density functional theory method and found to be oriented at an angle of 15.2° relative to the stacking axis (Figure 5b, bottom). This angular alignment met the requirement for J-type exciton coupling (i.e., <54.7°), providing compelling evidence for J-assembly formation. In particular, note that the single crystal of **SN1** yielded a fluorescence spectrum and Kubelka−Munk function ($F(R)$) displaying peak wavelengths essentially identical to those obtained for the nanoparticle suspension (1:19 v/v CH_3CN/H_2O; SI, Figure S19). This identity supported the claim that J-assembled nanoparticle formation was responsible for the enhanced fluorescence emission with the large bathochromic shifts. Taken together, the photophysical and structural results revealed the preassociation of **SN1** and **SN2** into J-assemblies prior to their interactions with Aβ species. In contrast, the other **SN** compounds did not form such J-assemblies in their preassociation states.

To elucidate a mechanism for the fluorescence responses of **SN2** and **SN4** to Aβ species, we performed morphological and spectroscopic investigations of the assemblies of **SN2** and **SN4** in the absence and presence of Aβ species. We examined whether the probe particles would disaggregate upon interacting with the hydrophobic Aβ species, which has been proposed in previous studies.[19,60] As shown in Figure 6a, **SN2** nanoparticles (2 μM in buffered aqueous solutions containing 20 mM *N*-(2-hydroxyethyl)piperazine-*N*′-ethanesulfonic acid (HEPES) and 150 mM NaCl, pH 7.4) yielded UV−vis absorption spectra displaying no discernable change after a 10 min incubation with Aβ_{42} aggregates that had been pre-incubated for 4 h. Longer incubation of **SN2** nanoparticles with Aβ_{42} aggregates for a period of a week did not lead to disassembly of the **SN2** J-nanoparticles, as revealed by the retention of the J-absorption band (SI, Figure S20). In addition, globular probe particles were found in the TEM images of **SN2** and **SN4**, each in the presence of Aβ_{42} aggregates (SI, Figure S21). These results indicated that the nanoparticle structures of the probes were retained upon their interaction with Aβ aggregates. Furthermore, no detectable difference of forming Aβ aggregates in the absence and presence of **SN2** or **SN4** was indicated by TEM and the dot blot assay (SI, Figures S22−S24), revealing that the **SN** probes did not interfere with Aβ aggregation. These results taken together indicated that the fluorescence responses of **SN2** and **SN4** to Aβ species were due to neither disaggregation of the probe J-assemblies nor probe-induced changes in the aggregation of Aβ and Aβ aggregates' morphology.

To gain insight into photophysical aspects of the mechanism of the fluorescence responses of **SN2** to Aβ species, fluorescence decay traces of **SN2** nanoparticles (2 μM) were acquired employing time-correlated single-photon counting techniques before and after incubation with Aβ_{42} aggregates in a buffered aqueous solution (pH 7.4, 20 mM HEPES, 150 mM NaCl). An increase in τ_{obs} upon the interaction of the **SN2** nanoparticles with the Aβ aggregates was evident, as shown in Figure 6b. Specifically, τ_{obs} increased from 0.84 ns in the absence of the Aβ_{42} aggregates to 1.32 ns after a 10 min incubation with the Aβ_{42} aggregates. Also, the values of k_r and k_{nr} correspondingly decreased, with a greater change observed for k_{nr} (Figure 6c). The greater decrease in k_{nr} enabled us to propose that Aβ species impeded nonradiative transitions of the probe nanoparticles. Similar behaviors were also observed for **SN4** (SI, Figure S25), corroborating this hypothesis.

To provide additional evidence for this hypothesis, we obtained fluorescence spectra of **SN2** and **SN4** with the addition of cetyltrimethylammonium bromide (CTAB), an amphiphilic surfactant, to form a hydrophobic layer shielding against fluorescence quenchers, such as water. This protective role of CTAB was expected to mimic the interaction with Aβ species. As expected, the addition of 100 mM CTAB into an aqueous solution of **SN2** nanoparticles evoked a ratiometric fluorescence response, similar to that observed for Aβ_{40} and Aβ_{42} (Figure 6d). Likewise, CTAB elicited a fluorescence turn-on of the **SN4** nanoparticles (Figure 6e). These results supported the idea that the fluorescence responses of **SN2** and **SN4** to Aβ species were due to abolition of deleterious quenching at the nanoparticle surface. An additional effect of the surface shielding was a hypsochromic shift of the fluorescence emission of the J-

DOI: 10.1021/acsomega.8b00286
ACS Omega 2018, 3, 5141−5154

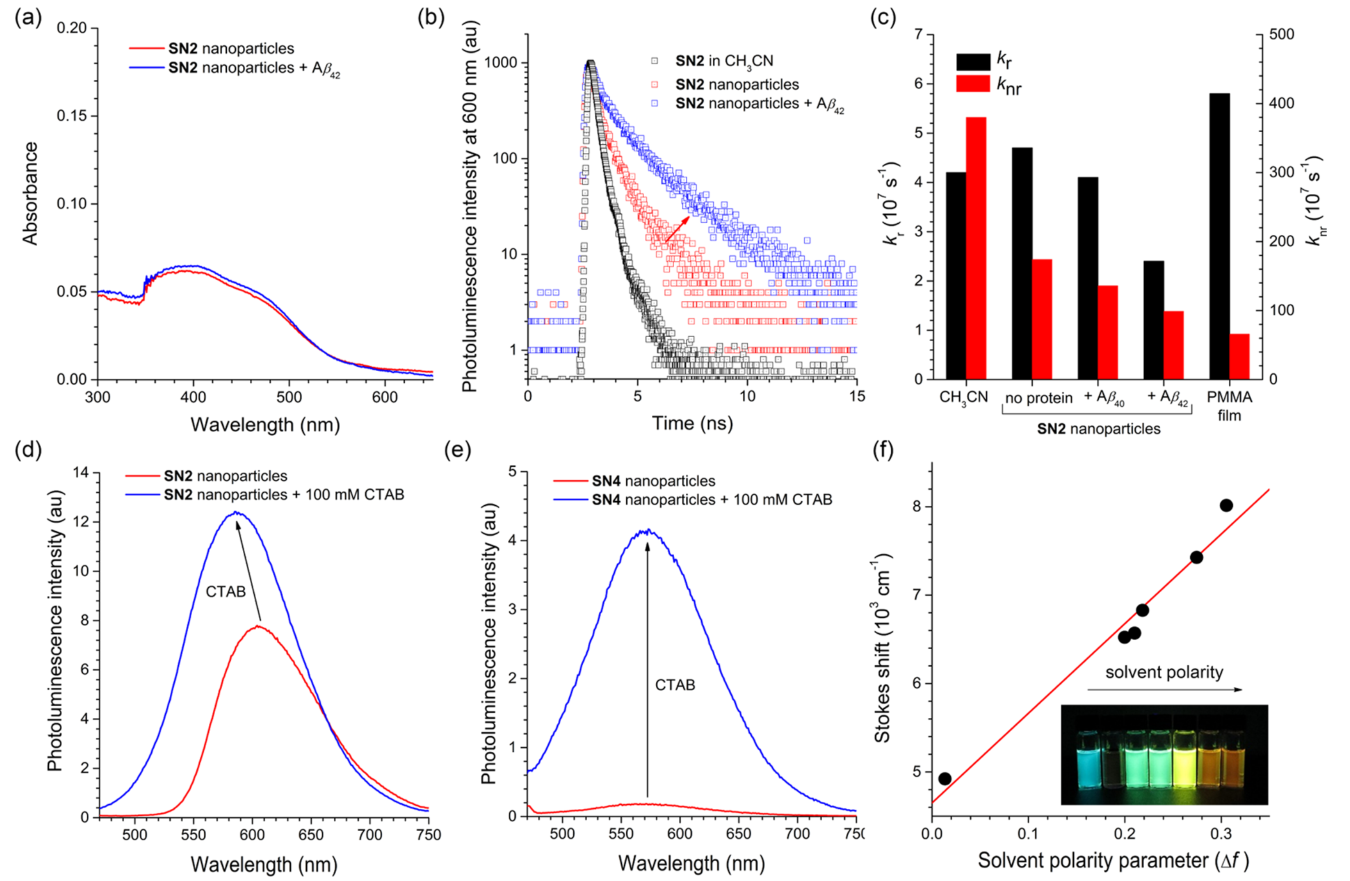

Figure 6. Photophysical responses of **SN2** to Aβ peptides. (a) UV−vis absorption spectra of **SN2** (2 μM) nanoparticles in the absence (red) and presence (blue) of Aβ_{42} (20 μM). (b) Photoluminescence decay traces of **SN2** in CH_3CN (2 μM, black) and of **SN2** nanoparticles (2 μM) in the absence (red) and presence (blue) of Aβ_{42} aggregates (20 μM), acquired after picosecond pulsed laser photoexcitation at a wavelength of 377 nm. (c) Comparisons of the radiative rate constants (k_r, black bars) and of the nonradiative rate constants (k_{nr}, red bars) of **SN2** at various conditions. (d) Photoluminescence spectra of **SN2** (2 μM) nanoparticles in the absence (red) and presence (blue) of 100 mM cetyltrimethylammonium bromide (CTAB). (e) Photoluminescence spectra of **SN4** (2 μM) nanoparticles in the absence (red) and presence (blue) of 100 mM CTAB. (f) The Lippert−Mataga plot showing the strong positive solvatochromism of **SN2**.

assemblies of **SN2** (Figure 6d). The chromic shift can be explained on the basis of hydrophobic interactions. The large positive solvatochromism of **SN2** corroborated this explanation (Figure 6f).

On the basis of the morphological and photophysical results, we devised a plausible mechanism for the fluorescence responses of **SN2** and **SN4** (Figure 7). According to this mechanism, the **SN2** molecules spontaneously formed J-assembled nanoparticles in the aqueous solutions. Although J-type exciton coupling enhanced the fluorescence intensities, emission quenching at the surface of the J-assemblies was still present, facilitating nonradiative deactivation. Aβ species effectively protected the surface against the nonradiative processes, producing turn-on fluorescence responses. In addition, the hydrophobic environment provided by the Aβ species induced a hypsochromic shift in the fluorescence emission. In the case of **SN4**, the probe did not self-organize into ordered molecular assemblies. The absence of J-assemblies resulted in fluorescence quenching of **SN4** nanoparticles, which is typically observed for organic molecules. Nonetheless, hydrophobic interactions of the **SN4** nanoparticles with Aβ aggregates turned on fluorescence emission to a considerable extent, an effect similar to that of **SN2**.

■ SUMMARY AND CONCLUSIONS

Prior to the current work, intermolecular interactions of lipophilic probes for Aβ species and the fluorescence outcomes of these interactions had not yet been studied because such studies were a significant challenge. Herein, we investigated preassociation behaviors of a series of D−A−D molecules (**SN** compounds) and utilized the preassemblies for monitoring Aβ aggregation. Of the five **SN** compounds investigated, **SN1** and **SN2** spontaneously formed highly fluorescent J-assembled nanoparticles in a buffered solution. Spectroscopic and X-ray crystallographic investigations specifically revealed the formation of intermolecular J-stacks. We successfully demonstrated the visualization of Aβ aggregation processes, employing J-type assemblies of **SN2** and non-J-type aggregates of **SN4**, which produced ratiometric and turn-on fluorescence signals, respectively. This example of the ratiometric fluorescence assay of Aβ aggregation using J-assembled nanoparticles is the first example, to the best of our knowledge. Photophysical and TEM investigations indicated that the probe nanoparticles did not undergo disaggregation upon interactions with Aβ species. Transient photophysical measurements provided evidence that hydrophobic interactions with Aβ species abolished fluorescence quenching at the particle surface. Experiments using a CTAB surfactant, an Aβ aggregate mimic, supported this notion.

DOI: 10.1021/acsomega.8b00286
ACS Omega 2018, 3, 5141−5154

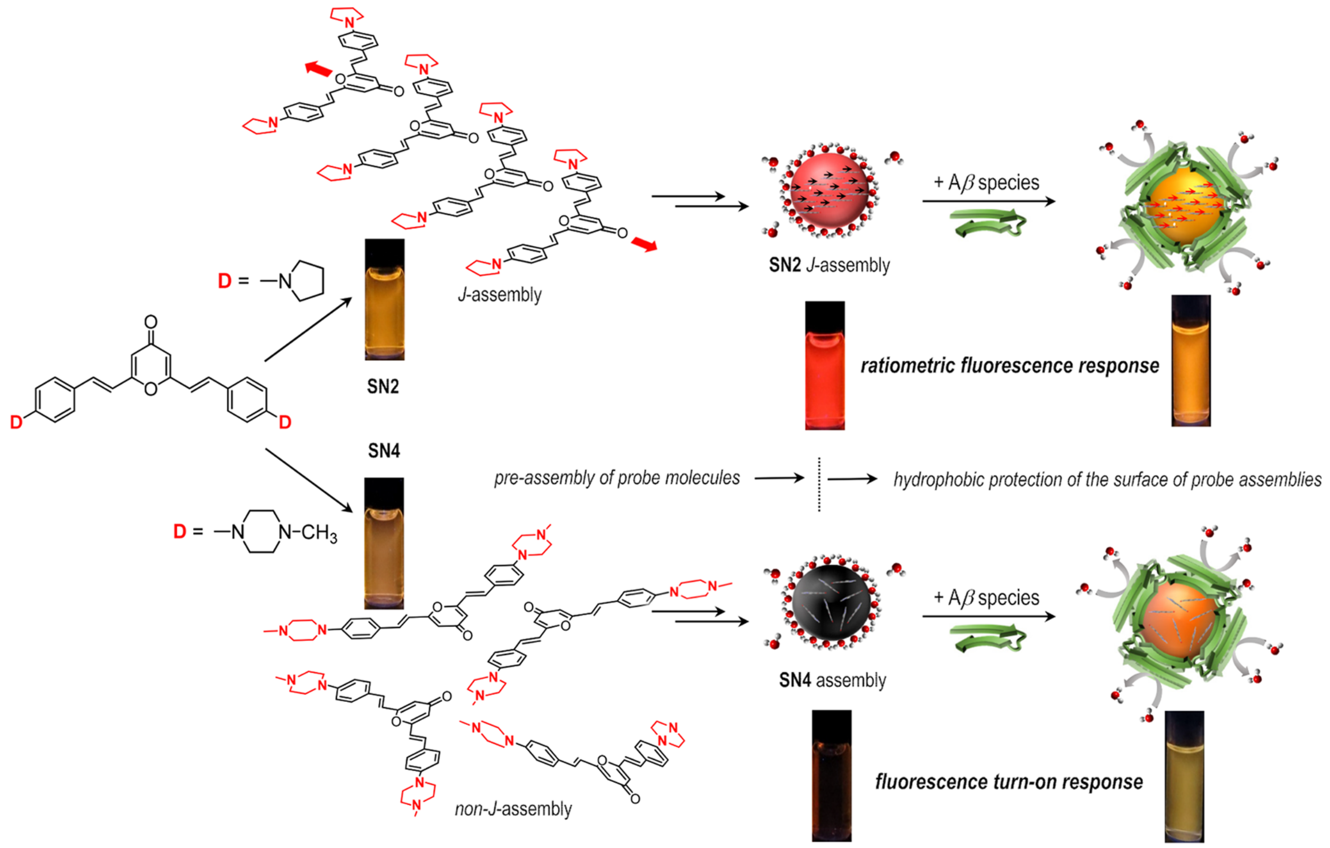

Figure 7. Schematic representation of a proposed mechanism for the fluorescence responses of the **SN2** (top) and **SN4** (bottom) nanoassemblies to Aβ species.

Overall, our studies provide a promising alternative to monitor Aβ aggregation pathways.

■ METHODS

Materials and General Methods. Commercially available chemicals were used as received unless otherwise stated. Piperazine-*N*,*N*′-bis(2-ethanesulfonic acid) (PIPES) and *N*-(2-hydroxyethyl)piperazine-*N*′-(2-ethanesulfonic acid) (HEPES) were purchased from Sigma-Aldrich. PIPES and HEPES buffer solutions were prepared in Milli-Q grade water from a Milli-Q Direct 16 system (18.2 MΩ·cm; Merck KGaA) and by adjusting the pH to 7.4 with standard KOH (45 wt %, Sigma-Aldrich) and HCl (1 N, Fluka) solutions. KCl (100 mM) and NaCl (150 mM) were included in the PIPES and HEPES solutions, respectively, to simulate the ionic strength of the biological milieu. Trace metal contamination was removed from buffers and solutions used for the experiments with peptides by treating the buffers and solutions with Chelex (Sigma-Aldrich). Aβ_{40} (DAEFRHDSGYEVHHQKLVFFAEDVGSNKGAIIGLMVGGVV) and Aβ_{42} (DAEFRHDSGYEVHHQKLVFFAEDVGSNKGAIIGLMVGGVVIA) were purchased from AnaSpec (Fremont, CA). Ubiquitin (MQIFVKTLTGKTITLEVEPSDTIENVKAKIQDKEGIPPDQQRLIFAGKQLEDGRTLSDYNIQKESTLHLVLRLRGG) was obtained from Sigma-Aldrich. The concentrations of Aβ and ubiquitin were determined using an Agilent, 8453 UV−vis spectrophotometer or a Cary 300 spectrophotometer. Stock solutions of the **SN** series were dissolved in CH_3CN (Sigma-Aldrich, spectrophotometric grade) or dimethyl sulfoxide (DMSO) (Sigma-Aldrich, Biotech grade) to a concentration of 10 mM and stored frozen. The solutions were thawed before spectroscopic measurements were taken. Typically, a volume of 3 μL of the **SN** stock solution was delivered to 3.0 mL of CH_3CN or the buffer solutions, resulting in **SN** compounds with a concentration of 10 μM. ^{1}H and ^{13}C{^{1}H} NMR spectra were collected with Bruker, Ultrashield 500 and 300 plus NMR spectrometers. Chemical shifts were referenced to $(CH_3)_4Si$. High-resolution mass spectra (positive mode, fast atom bombardment (FAB), *m*-nitrobenzyl alcohol (*m*-NBA)) were obtained by employing a JEOL, JMS-600W mass spectrometer. C, H, and N analyses were performed by employing Thermo Fisher Scientific, Flash1112 and Flash2000 elemental analyzers.

Synthesis of ***SN1***. 2,6-Dimethyl-γ-pyrone (2.00 g, 16.1 mmol) and 4-(*N*,*N*-dimethylamino)benzaldehyde (4.81 g, 32.2 mmol) were added into a 100 mL two-neck round-bottom flask. Anhydrous ethanol (60 mL) was delivered into the flask using a glass syringe under an Ar atmosphere. Sodium ethoxide (18 mL, 48 mmol; 21 wt % in ethanol, Sigma-Aldrich) was added slowly into the solution using a disposable syringe. The reaction mixture was refluxed for 48 h under an Ar atmosphere. After cooling to room temperature, the solution was concentrated under a reduced pressure. Silica gel column purification was performed with increasing polarity of eluents from 100% CH_2Cl_2 to 19:1 v/v CH_2Cl_2/CH_3OH. An orange solid was obtained with a yield of 56%. R_f = 0.2 (19:1 v/v EtOAc/CH_3OH). ^{1}H NMR (300 MHz, $CDCl_3$) δ (ppm): 3.04 (s, 12H), 6.16 (s, 2H), 6.52 (d, J = 15.9 Hz, 2H), 6.72 (d, J = 8.7 Hz, 4H), 7.41 (d, J = 15.9 Hz, 2H), 7.47 (d, J = 9.0 Hz, 4H). ^{13}C{^{1}H} NMR (126 MHz, CD_2Cl_2) δ (ppm): 40.50, 112.46, 112.52, 115.23, 123.44, 129.48, 136.28, 151.96, 162.53, 180.34. HR MS (FAB, *m*-NBA): calcd for

DOI: 10.1021/acsomega.8b00286
ACS Omega 2018, 3, 5141−5154

$C_{25}H_{27}N_2O_2$ ([M + H]$^+$), 387.2073; found: 387.2069. Anal. calcd for $C_{25}H_{26}N_2O_2$: C, 77.69; H, 6.78; N, 7.25. Found: C, 77.49; H, 6.72; N, 7.29.

*Synthesis of **SN2**.* **SN2** was synthesized using the same procedure as was used to synthesize **SN1**, except that 4-(1-pyrrolidinyl)benzaldehyde (4.99 g, 28.5 mmol) was used in the place of 4-(*N,N*-dimethylamino)benzaldehyde. An orange solid was obtained in a yield of 8%. R_f = 0.2 (CH_2Cl_2). ^{1}H NMR (300 MHz, $CDCl_3$) δ (ppm): 2.04 (m, 8H), 3.36 (m, 8H), 6.15 (s, 2H), 6.48 (d, J = 15.9 Hz, 2H), 6.56 (d, J = 8.7 Hz, 4H), 7.40 (d, J = 16.2 Hz, 2H), 7.45 (d, J = 8.7 Hz, 4H). ^{13}C{^{1}H} NMR (CD_2Cl_2, 126 MHz) δ (ppm): 26.00, 48.13, 112.12, 112.26, 114.41, 122.72, 129.70, 136.72, 149.56, 162.84, 180.57. HR MS (FAB, *m*-NBA): calcd for $C_{29}H_{31}N_2O_2$ ([M + H]$^+$), 439.2386; found: 439.2379.

*Synthesis of **SN3**.* **SN3** was synthesized using the same procedure as was used to synthesize **SN1**, except that 4-(*N,N*-diphenylamino)benzaldehyde (4.41 g, 16.1 mmol) was used in the place of 4-(*N,N*-dimethylamino)benzaldehyde. An orange solid was obtained in a yield of 40%. R_f = 0.2 (1:1 v/v CH_2Cl_2/hexane). ^{1}H NMR (300 MHz, $CDCl_3$) δ (ppm): 6.22 (s, 2H), 6.59 (d, J = 15.9 Hz, 2H), 7.06 (m, 8H), 7.14 (m, 8H), 7.30 (m, 8H), 7.39 (m, 6H). ^{13}C{^{1}H} NMR (126 MHz, CD_2Cl_2) δ (ppm): 113.66, 118.07, 122.49, 124.44, 125.83, 128.90, 129.08, 130.00, 135.58, 147.58, 149.84, 162.05, 180.22. HR MS (FAB, *m*-NBA): calcd for $C_{45}H_{35}N_2O_2$ ([M + H]$^+$), 635.2699; found: 635.2690. Anal. calcd for $C_{45}H_{34}N_2O_2$: C, 85.15; H, 5.40; N, 4.41. Found: C, 84.53; H, 5.71; N, 4.42.

*Synthesis of **SN4**.* **SN4** was synthesized using the same procedure as was used to synthesize **SN1**, except that 4-(4-methylpiperazinyl)benzaldehyde (3.29 g, 16.1 mmol) was used in the place of 4-(*N,N*-dimethylamino)benzaldehyde. An orange solid was obtained in a yield of 36%. R_f = 0.1 (5:1 v/v CH_2Cl_2/CH_3OH). ^{1}H NMR (300 MHz, $CDCl_3$) δ (ppm): 2.37 (s, 6H), 2.59 (m, 8H), 3.33 (m, 8H), 6.20 (s, 2H), 6.57 (d, J = 15.9 Hz, 2H), 6.92 (d, J = 8.7 Hz, 4H), 7.42 (d, J = 16.2 Hz, 2H), 7.48 (d, J = 9.0 Hz, 4H). ^{13}C{^{1}H} NMR (126 MHz, CD_2Cl_2) δ (ppm): 46.42, 48.35, 55.38, 113.06, 115.41, 116.66, 125.97, 129.36, 135.99, 152.73, 162.35, 180.38. HR MS (FAB, *m*-NBA): calcd for $C_{31}H_{37}N_4O_2$ ([M + H]$^+$), 497.2917; found: 497.2919. Anal. calcd for $C_{31}H_{36}N_4O_2$: C, 74.97; H, 7.31; N, 11.28. Found: C, 74.83; H, 7.44; N, 11.27.

*Synthesis of **SN5**.* **SN5** was synthesized using the same procedure as was used to synthesize **SN1**, except that 4-(4-morpholinyl)benzaldehyde (3.08 g, 16.1 mmol) was used in the place of 4-(*N,N*-dimethylamino)benzaldehyde. A yellow solid was obtained in a yield of 45%. R_f = 0.3 (19:1 v/v CH_2Cl_2/CH_3OH). ^{1}H NMR (300 MHz, $CDCl_3$) δ (ppm): 3.27 (m, 8H), 3.88 (m, 8H), 6.20 (s, 2H), 6.59 (d, J = 15.9 Hz, 2H), 6.92 (d, J = 9.0 Hz, 4H), 7.41 (d, J = 5.9 Hz, 2H), 7.50 (d, J = 8.7 Hz, 4H). ^{13}C{^{1}H} NMR (126 MHz, CD_2Cl_2) δ (ppm): 48.73, 67.18, 113.26, 115.30, 117.07, 126.58, 129.36, 135.87, 152.78, 162.27, 180.36. HR MS (FAB, *m*-NBA): calcd for $C_{29}H_{31}N_2O_4$ ([M + H]$^+$), 471.2284; found: 471.2288. Anal. calcd for $C_{29}H_{30}N_2O_4$: C, 74.02; H, 6.43; N, 5.95. Found: C, 73.92; H, 6.48; N, 5.95.

X-ray Crystallography. Crystals suitable for X-ray crystallography were obtained by performing a slow diffusion of hexane onto a dichloromethane solution of 0.15 M **SN1**. Single crystals of **SN1** were picked from the solution with a nylon loop (Hampton Research Co.) at room temperature and mounted on a goniometer head in an N_2 cryostream. Data from a single **SN1** crystal were collected using a Bruker, SMART APEX II CCD diffractometer equipped with a monochromator for an Mo Kα (λ = 0.71073 Å) beam. The charge-coupled device data were integrated and scaled using the Bruker-SAINT software package, and the structure was solved and refined with SHEXTL V 6.12. Hydrogen atoms were placed on the calculated positions. Nonhydrogen atoms were refined with anisotropic thermal parameters. Crystal data for **SN1**: $C_{25}H_{26}N_2O_2$, monoclinic, $P2_1/n$, Z = 4, a = 7.8531(5), b = 7.4811(4), c = 34.767(2) Å, β = 91.880(3)°, V = 2041.5(2) Å^3, μ = 0.080 mm^{-1}, ρ_{calcd} = 1.257 g cm^{-3}, R_1 = 0.0800, wR_2 = 0.1275 for 4023 unique reflections, 267 variables. These crystallographic data for **SN1** are also summarized in SI, Table S1, and Table S2 in the SI lists the selected bond distances and angles. CCDC 1558038 for **SN1** contains the supporting crystallographic data for this paper.

Preparation of Nanoparticles of SN1−SN5. A nanoparticle suspension of each **SN** compound was prepared by slowly adding Milli-Q grade water into a vigorously stirred CH_3CN solution containing the **SN** compound until the total volume of the mixture reached 10 mL. The final concentration of the **SN** compound was 10 μM. The stirred solution became cloudy when the water volume fraction exceeded 90 vol %. Typically, water volume fractions of greater than 97.5% were prepared for spectroscopic measurements.

Preparation of Aβ Aggregates and Ubiquitin. Aβ peptides were dissolved in hexafluoro-2-propanol (HFIP) and sonicated for 30 min. After removal of HFIP, the Aβ peptides were redissolved in NH_4OH (1% w/v, aq; 10 μL) and then diluted in doubly distilled water (ddH_2O). The concentration of Aβ was determined by measuring the absorbance of the solution at 280 nm (ε = 1450 M^{-1} cm^{-1} for Aβ_{40}; ε = 1490 M^{-1} cm^{-1} for Aβ_{42}). A buffered solution (20 mM HEPES, pH 7.4, 150 mM NaCl) was used to prepare the Aβ samples. The Aβ samples (20 μM) were incubated at 37 °C for various durations with constant agitation. The ubiquitin peptide was prepared by dissolving it in ddH_2O. The concentration of ubiquitin was determined by measuring the absorbance of the solution at 280 nm (ε = 1280 M^{-1} cm^{-1}). The ubiquitin solution was diluted to 20 μM with the buffered solution (i.e., 20 mM HEPES, pH 7.4, 150 mM NaCl).

Steady-State Photoluminescence Measurements. Photoluminescence spectra were obtained using a Photon Technology International, Quanta Master 400 scanning spectrofluorometer at room temperature (CH_3CN) or at 37 °C (buffered solutions). The temperature was maintained by employing a water circulator. The 10 μM solutions were used for the measurements, otherwise mentioned. Excitation wavelengths were 417 nm (**SN1**), 399 nm (**SN2**), 409 nm (**SN3**), 404 nm (**SN4**), and 396 nm (**SN5**). The fluorescence quantum yields (Φ_fs) were relatively determined according to the following equation: $\Phi_f = \Phi_{f,ref} \times (I/I_{ref}) \times (A_{ref}/A) \times (n/n_{ref})^2$, where A, I, and n are the absorbance at the excitation wavelength, integrated photoluminescence intensity, and the refractive index of the solvent, respectively. 9,10-Diphenylanthracene in toluene was used as the external reference ($\Phi_{f,ref}$ = 1.00).[73]

Fluorescence Lifetime Measurements. Solutions (2 or 10 μM) in Ar-saturated CH_3CN or buffered solutions were used for determination of the fluorescence lifetime (τ_{obs}). Photoluminescence decay traces were acquired on the basis of the time-correlated single-photon counting techniques using a PicoQuant, FluoTime 200 instrument after picosecond pulsed laser excitation. A 377 nm diode laser (PicoQuant) was used as the excitation source. The photoluminescence signals at the emission peak wavelengths were obtained through an automated motorized monochromator. Photoluminescence decay profiles were analyzed (OriginPro 8.0, OriginLab) using single- or

DOI: 10.1021/acsomega.8b00286
ACS Omega 2018, 3, 5141−5154

double-exponential decay models. In the case of biphasic decays, τ_{obs} values were calculated from the relationship $\tau_{obs} = \sum A_i\tau_i^2/\sum A_i\tau_i$ (i = 1−2), where A_i and τ_i are the preexponential factor and the time constant, respectively.

Dynamic Light Scattering Experiments. Distributions of particle diameters of 10 μM nanoparticle suspensions were determined through dynamic light scattering (DLS) experiments using a Photal Otsuka Electronics, ELS-Z1000 instrument at room temperature. Data analyses were performed by employing the software provided by the manufacturer.

Field-Emission Scanning Electron Microscope Experiments. An aliquot of 10 μM nanoparticle suspensions was placed on a 1 cm × 1 cm glass substrate and dried under dark. The field-emission scanning electron microscope images of the nanoparticles were obtained using a Carl Zeiss, SUPRA 55VP equipment after platinum coating (120 s) using a Leica, EM ACE200.

Determination of the Partition Coefficient (clog *P*). The same volumes of *n*-octanol and a buffered solution (10 mM PBS, pH 7.4) were stirred for 24 h and transferred into a separatory funnel for complete phase separation at room temperature (presaturation process). **SN** solutions (20 μM) in *n*-octanol (saturated with water) were used for determination of molar absorbance (ε) values by employing the Beer−Lambert law. A 15 mL of *n*-octanol and a magnetic stir bar were put into a 40 mL vial. A 15 mL of a PBS solution was added into the vial, after which the saturation and the phase separation process were repeated. The concentration of the **SN** compound in the organic layer (C_o) was quantified by UV−vis absorbance spectroscopy. The concentration of the **SN** compound in the aqueous layer (C_w) was calculated from the equation $C_w = 20\ \mu M - C_o$. The partition coefficient (clog P) was determined from the relationship clog $P = \log(C_o/C_w)$.

Solvatochromism. Fluorescence spectra of 10 μM **SN2** solutions were acquired under a photoexcitation wavelength 399 nm, and peak wavenumbers of the spectra were determined. The Lippert−Mataga plot was constructed as a function of polarity parameter (f); $f = ((\varepsilon - 1)/(2\varepsilon + 1)) - ((n^2 - 1)/(2n^2 + 1))$ (ε, dielectric constant; n, refractive index). f: toluene, 0.0135; chloroform, 0.148; ethyl acetate, 0.200; 2-methyltetrahydrofuran, 0.210; dichloromethane, 0.218; *N*,*N*-dimethylformamide, 0.275; acetonitrile, 0.305.

ThT Assay. The kinetics of the formation of β-sheet-rich Aβ aggregates was monitored by applying the ThT assay. Each Aβ sample (20 μM), obtained after different incubation time points at 37 °C with constant agitation (in 20 mM HEPES, pH 7.4, 150 mM NaCl), was treated with 20 μM ThT. After 20 min, the fluorescence intensity of ThT was measured using a Molecular Devices, SpectraMax M5e microplate reader at λ_{ex} = 440 nm and λ_{em} = 490 nm.

Transmission Electron Microscopy (TEM) Experiments. Aβ samples for TEM measurements were prepared following previously reported methods.[83−87] Glow discharged grids (Formvar/Carbon 300 mesh, Electron Microscopy Sciences, Hatfield, PA) were treated with samples (5 μL) of (i) **SN** compound-free Aβ aggregates and (ii) Aβ aggregates incubated with the **SN** compounds for 2 min at room temperature. Excess sample was removed with filter paper, and the grids were washed with ddH_2O three times. Each grid was stained with uranyl acetate (1% w/v ddH_2O; 5 μL) for 1 min. Uranyl acetate was blotted off, and the grids were dried for at least 20 min at room temperature. Images of samples were taken using a JEOL, JEM-2100 transmission electron microscope (200 kV; 25 000× magnification; UCRF, Ulsan, Republic of Korea).

Dot Blot Assay. Aβ aggregates with and without treatment of **SN2** and **SN4** (2 μL), generated with various durations of preincubation, were spotted on a nitrocellulose membrane, and the membrane was blocked with a solution of bovine serum albumin (BSA; 3% w/v; RMBIO, Missoula, MT) in Tris-buffered saline containing 0.01% Tween 20 (TBS-T) at room temperature for 1.5 h. Then, the membrane was incubated with a primary antibody, 6E10 (1:2000, Covance, Princeton, NJ) or A11 (1:2500, Millipore, Billerica, MA) in a solution of 2% w/v BSA in TBS-T for 1.5 h at room temperature. After washing with TBS-T three times (7 min each), the horseradish peroxidase-conjugated goat anti-mouse (for 6E10) or goat anti-rabbit (for A11) secondary antibody (1:5000, Cayman Chemical Company for 6E10; 1:2500, Promega for A11) in the solution of BSA (2% w/v in TBS-T) was added to the membrane and incubated for 1 h at room temperature. A homemade ECL kit[88] was used to visualize the results on a Bio-Rad, ChemiDoc MP Imaging System. The same membrane was stripped by treating it with hydrogen peroxide (H_2O_2) for 30 min at room temperature, washed four times with TBS-T for 10 min each, blocked with the solution of 3% w/v BSA in TBS-T, and incubated with the primary antibodies (6E10 and A11).

Images of Aβ Aggregates by Our Probes. Large-sized Aβ aggregates were generated by incubating Aβ peptides (370 μM for Aβ_{42}; 260 μM for Aβ_{40}) for 36 h at 37 °C with constant agitation. The resulting Aβ species were treated with **SN2** and **SN4** (37 μM for Aβ_{42}; 26 μM for Aβ_{40}; final concentration of DMSO, 1% v/v) for 10 min prior to imaging using a confocal microscope [Carl Zeiss, LSM 780 (KAIST Analysis Center for Research Advancement, KAIST, Daejeon, Republic of Korea)]. The images were obtained with a 405 nm laser (2.0% power; 0.39 μs as the pixel dwell; 89.6 μm as the pinhole size; 63× objective). The emission was collected from 550 to 630 nm for **SN2** and from 480 to 600 nm for **SN4**.

Preparation of Cell Lysates. N2a APPwt neuroblastoma cells were the generous gift of Professor Gopal Thinakaran (University of Chicago). Cells were seeded in a six-well plate and incubated for 48 h. After removing media, the cells were washed with PBS and lysed with radioimmunoprecipitation assay lysis buffer (50 mM Tris, 150 mM NaCl, 0.1% sodium dodecyl sulfate (SDS), 0.5% sodium deoxycholate, 1% Triton X-100) containing 1× protease cocktail (Sigma-Aldrich) and 1 mM phenylmethane sulfonyl fluoride. The total protein concentration in cell lysates was determined by the bicinchoninic acid assay.

Fluorescence Detection of Aβ Aggregates. The fluorescence responses of each probe (**SN1**−**SN5**; 2 μM; final concentration of DMSO, 1% v/v) to Aβ_{40}, Aβ_{42}, and ubiquitin (20 μM) were recorded after 10 min incubation in 20 mM HEPES, pH 7.4, 150 mM NaCl (λ_{ex} = 417, 399, 409, 404, and 396 nm for **SN1**, **SN2**, **SN3**, **SN4**, and **SN5**, respectively).

Cell Viability Assay. N2a neuroblastoma cell line was purchased from the American Type Culture Collection (ATCC, Manassas, VA). The cell line was maintained in media containing 50% Dulbecco's modified Eagle's medium and 50% Opti-MEM (Gibco), supplemented with 10% fetal bovine serum (Sigma-Aldrich), 2 mM glutamine, 100 U mL^{-1} penicillin, and 100 mg mL^{-1} streptomycin (Gibco). The cells were grown and maintained at 37 °C in a humidified atmosphere with 5% CO_2. Cell viability upon treatment of the **SN** compounds was determined using the MTT assay (MTT = 3-(4,5-dimethyl-2-thiazolyl)-2,5-diphenyl-2*H*-tetrazolium bromide, Sigma-Al-

DOI: 10.1021/acsomega.8b00286
ACS Omega 2018, 3, 5141−5154

drich). N2a cells were seeded in a 96-well plate (8000 and 3000 cells in 100 μL per well for 1 and 24 h incubation, respectively). The cells were treated with compounds (1, 2, and 5 μM, 1% v/v final DMSO concentration) and incubated for 1 and 24 h. After incubation, MTT (25 μL; 5 mg mL^{-1} in phosphate-buffered saline (PBS, pH 7.4, Gibco)) was added to each well and the plate was incubated for 4 h at 37 °C. Formazan produced by the cells was solubilized using an acidic solution of *N*,*N*-dimethylformamide (50% v/v, aq) and sodium dodecyl sulfate (SDS, 20% w/v) overnight at room temperature in the dark. The absorbance was measured at 600 nm using a microplate reader. Cell viability was calculated relative to cells treated with an equivalent amount of DMSO. All experiments were carried out in triplicate.

■ ASSOCIATED CONTENT

Supporting Information

The Supporting Information is available free of charge on the ACS Publications website at DOI: 10.1021/acsomega.8b00286.

Experimental details; ^{1}H and ^{13}C{^{1}H} NMR spectra of the **SN** compounds, fluorescence responses of **SN1**, **SN3**, and **SN5** to Aβ_{42} and Aβ_{40} species, fluorescence images of Aβ aggregates treated with **SN2** and **SN4**, normalized chemiluminescence intensities from the dot blots, fluorescence responses of the **SN** compounds to ubiquitin, fluorescence responses of **SN2** and **SN4** to Aβ_{40} species in the presence of ubiquitin or in cell lysates, viability of N2a cells treated with **SN2** and **SN4**, photoluminescence spectra of **SN2** obtained at various conditions, comparisons of the UV−vis absorption and photoluminescence spectra of **SN1**, **SN3**, **SN4**, and **SN5**, the Kubelka−Munk function and a photoluminescence spectrum of a single crystal of **SN1**, stability of **SN2** J-assemblies in the presence of Aβ_{42} aggregates, TEM images showing the retention of nanoparticle structures of the probes during the aggregation of Aβ_{42}, TEM images of Aβ_{42} and Aβ_{40} aggregates preincubated for various durations, aggregation kinetics and conformations of Aβ_{40} and Aβ_{42} aggregates upon treatment of **SN2** and **SN4**, and changes in the k_r and k_{nr} values of the **SN4** nanoparticles at various conditions (Figures S1−S25); crystallographic data and selected bond lengths and bond angles for the **SN1** crystal (Tables S1 and S2) (PDF)

Crystallographic data (CIF)

■ AUTHOR INFORMATION

Corresponding Authors

*E-mail: jaeheung@dgist.ac.kr (J.C.).
*E-mail: miheelim@kaist.ac.kr (M.H.L.).
*E-mail: odds2@ewha.ac.kr (Y.Y.).

ORCID

Jaeheung Cho: 0000-0002-2712-4295
Mi Hee Lim: 0000-0003-3377-4996
Youngmin You: 0000-0001-5633-6599

Author Contributions

#Institutional affiliations where research for the paper was conducted (for H.J.L., E.N., and M.H.L.): Department of Chemistry, Ulsan National Institute of Science and Technology (UNIST), Ulsan 44919, Republic of Korea and Department of Chemistry, Korea Advanced Institute of Science and Technology (KAIST), Daejeon 34141, Republic of Korea.

Author Contributions

⊥S.K., H.J.L., and E.N. contributed equally to this work.

Notes

The authors declare no competing financial interest.

■ ACKNOWLEDGMENTS

This work was supported by a grant from the Samsung Research Funding Center for Future Technology (SRFC-MA1301-01 to Y.Y.), the National Research Foundation of Korea (NRF-2017R1A2B3002585 and NRF-2016R1A5A1009405 to M.H.L. and NRF-2017R1A2B4005441 to J.C.), the Korea Advanced Institute of Science and Technology (to M.H.L.), and the Ministry of Science and ICT (DGIST R&D Program 18-BD-0403 to J.C.).

■ REFERENCES

(1) Wetzel, R. Kinetics and thermodynamics of amyloid fibril assembly. *Acc. Chem. Res.* **2006**, *39*, 671−679.

(2) Harper, J. D.; Lansbury, P. T., Jr. Models of amyloid seeding in Alzheimer's disease and scrapie: mechanistic truths and physiological consequences of the time-dependent solubility of amyloid proteins. *Annu. Rev. Biochem.* **1997**, *66*, 385−407.

(3) Berhanu, W. M.; Hansmann, U. H. E. Structure and dynamics of amyloid-β segmental polymorphisms. *PLoS One* **2012**, *7*, No. e41479.

(4) Garzon-Rodriguez, W.; Sepulveda-Becerra, M.; Milton, S.; Glabe, C. G. Soluble amyloid Aβ-(1−40) exists as a stable dimer at low concentrations. *J. Biol. Chem.* **1997**, *272*, 21037−21044.

(5) Bernstein, S. L.; Dupuis, N. F.; Lazo, N. D.; Wyttenbach, T.; Condron, M. M.; Bitan, G.; Teplow, D. B.; Shea, J.-E.; Ruotolo, B. T.; Robinson, C. V.; Bowers, M. T. Amyloid-β protein oligomerization and the importance of tetramers and dodecamers in the aetiology of Alzheimer's disease. *Nat. Chem.* **2009**, *1*, 326−331.

(6) Ono, K.; Condron, M. M.; Teplow, D. B. Structure-neurotoxicity relationships of amyloid β-protein oligomers. *Proc. Natl. Acad. Sci. U.S.A.* **2009**, *106*, 14745−14750.

(7) Beck, M. W.; Pithadia, A. S.; DeToma, A. S.; Korshavn, K. J.; Lim, M. H. Ligand Design to Target and Modulate Metal−Protein Interactions in Neurodegenerative Diseases. In *Ligand Design in Medicinal Inorganic Chemistry*; John Wiley & Sons, Ltd: 2014; pp 257−286.

(8) Lee, S. J. C.; Nam, E.; Lee, H. J.; Savelieff, M. G.; Lim, M. H. Towards an understanding of amyloid-β oligomers: characterization, toxicity mechanisms, and inhibitors. *Chem. Soc. Rev.* **2017**, *46*, 310−323.

(9) Faller, P.; Hureau, C.; Berthoumieu, O. Role of metal ions in the self-assembly of the Alzheimer's amyloid-β peptide. *Inorg. Chem.* **2013**, *52*, 12193−12206.

(10) Rajasekhar, K.; Chakrabarti, M.; Govindaraju, T. Function and toxicity of amyloid beta and recent therapeutic interventions targeting amyloid beta in Alzheimer's disease. *Chem. Commun.* **2015**, *51*, 13434−13450.

(11) Kotler, S. A.; Brender, J. R.; Vivekanandan, S.; Suzuki, Y.; Yamamoto, K.; Monette, M.; Krishnamoorthy, J.; Walsh, P.; Cauble, M.; Holl, M. M. B.; Marsh, E. N. G.; Ramamoorthy, A. High-resolution NMR characterization of low abundance oligomers of amyloid-β without purification. *Sci. Rep.* **2015**, *5*, No. 11811.

(12) Bruggink, K. A.; Jongbloed, W.; Biemans, E. A. L. M.; Veerhuis, R.; Claassen, J. A. H. R.; Kuiperij, H. B.; Verbeek, M. M. Amyloid-β oligomer detection by ELISA in cerebrospinal fluid and brain tissue. *Anal. Biochem.* **2013**, *433*, 112−120.

(13) Savelieff, M. G.; Lee, S.; Liu, Y.; Lim, M. H. Untangling amyloid-β, tau, and metals in Alzheimer's disease. *ACS Chem. Biol.* **2013**, *8*, 856−865.

(14) Koffie, R. M.; Meyer-Luehmann, M.; Hashimoto, T.; Adams, K. W.; Mielke, M. L.; Garcia-Alloza, M.; Micheva, K. D.; Smith, S. J.; Kim, M. L.; Lee, V. M.; Hyman, B. T.; Spires-Jones, T. L. Oligomeric amyloid β associates with postsynaptic densities and correlates with excitatory

synapse loss near senile plaques. *Proc. Natl. Acad. Sci. U.S.A.* **2009**, *106*, 4012−4017.
(15) Shankar, G. M.; Li, S.; Mehta, T. H.; Garcia-Munoz, A.; Shepardson, N. E.; Smith, I.; Brett, F. M.; Farrell, M. A.; Rowan, M. J.; Lemere, C. A.; Regan, C. M.; Walsh, D. M.; Sabatini, B. L.; Selkoe, D. J. Amyloid-β protein dimers isolated directly from Alzheimer's brains impair synaptic plasticity and memory. *Nat. Med.* **2008**, *14*, 837−842.
(16) Lesné, S.; Koh, M. T.; Kotilinek, L.; Kayed, R.; Glabe, C. G.; Yang, A.; Gallagher, M.; Ashe, K. H. A specific amyloid-β protein assembly in the brain impairs memory. *Nature* **2006**, *440*, 352−357.
(17) Lambert, M. P.; Barlow, A. K.; Chromy, B. A.; Edwards, C.; Freed, R.; Liosatos, M.; Morgan, T. E.; Rozovsky, I.; Trommer, B.; Viola, K. L.; Wals, P.; Zhang, C.; Finch, C. E.; Krafft, G. A.; Klein, W. L. Diffusible, nonfibrillar ligands derived from A$\beta_{1\text{-}42}$ are potent central nervous system neurotoxins. *Proc. Natl. Acad. Sci. U.S.A.* **1998**, *95*, 6448−6453.
(18) Burnham, S. C.; Faux, N. G.; Wilson, W.; Laws, S. M.; Ames, D.; Bedo, J.; Bush, A. I.; Doecke, J. D.; Ellis, K. A.; Head, R.; Jones, G.; Kiiveri, H.; Martins, R. N.; Rembach, A.; Rowe, C. C.; Salvado, O.; Macaulay, S. L.; Masters, C. L.; Villemagne, V. L. A blood-based predictor for neocortical Aβ burden in Alzheimer's disease: results from the AIBL study. *Mol. Psychiatry* **2014**, *19*, 519−526.
(19) Crouch, P. J.; Harding, S.-M. E.; White, A. R.; Camakaris, J.; Bush, A. I.; Masters, C. L. Mechanisms of Aβ mediated neurodegeneration in Alzheimer's disease. *Int. J. Biochem. Cell Biol.* **2008**, *40*, 181−198.
(20) Hu, Y.; Su, B.; Kim, C.-S.; Hernandez, M.; Rostagno, A.; Ghiso, J.; Kim, J. R. A strategy for designing a peptide probe for detection of β-amyloid oligomers. *ChemBioChem* **2010**, *11*, 2409−2418.
(21) Lee, J.; Culyba, E. K.; Powers, E. T.; Kelly, J. W. Amyloid-β forms fibrils by nucleated conformational conversion of oligomers. *Nat. Chem. Biol.* **2011**, *7*, 602−609.
(22) Morgado, I.; Wieligmann, K.; Bereza, M.; Rönicke, R.; Meinhardt, K.; Annamalai, K.; Baumann, M.; Wacker, J.; Hortschansky, P.; Malešević, M.; Parthier, C.; Mawrin, C.; Schiene-Fischer, C.; Reymann, K. G.; Stubbs, M. T.; Balbach, J.; Görlach, M.; Horn, U.; Fändrich, M. Molecular basis of β-amyloid oligomer recognition with a conformational antibody fragment. *Proc. Natl. Acad. Sci. U.S.A.* **2012**, *109*, 12503−12508.
(23) Takahashi, T.; Mihara, H. FRET detection of amyloid β-peptide oligomerization using a fluorescent protein probe presenting a pseudo-amyloid structure. *Chem. Commun.* **2012**, *48*, 1568−1570.
(24) Teoh, C. L.; Su, D.; Sahu, S.; Yun, S.-W.; Drummond, E.; Prelli, F.; Lim, S.; Cho, S.; Ham, S.; Wisniewski, T.; Chang, Y.-T. Chemical fluorescent probe for detection of Aβ oligomers. *J. Am. Chem. Soc.* **2015**, *137*, 13503−13509.
(25) Selkoe, D. J. Alzheimer's disease: genes, proteins, and therapy. *Physiol. Rev.* **2001**, *81*, 741−766.
(26) Xu, M.-m.; Ren, W.-m.; Tang, X.-c.; Hu, Y.-h.; Zhang, H.-y. Advances in development of fluorescent probes for detecting amyloid-β aggregates. *Acta Pharmacol. Sin.* **2016**, *37*, 719−730.
(27) Staderini, M.; Martín, M. A.; Bolognesi, M. L.; Menéndez, J. C. Imaging of β-amyloid plaques by near infrared fluorescent tracers: a new frontier for chemical neuroscience. *Chem. Soc. Rev.* **2015**, *44*, 1807−1819.
(28) Cui, M. Past and recent progress of molecular imaging probes for β-amyloid plaques in the brain. *Curr. Med. Chem.* **2014**, *21*, 82−112.
(29) Urbanc, B.; Cruz, L.; Le, R.; Sanders, J.; Ashe, K. H.; Duff, K.; Stanley, H. E.; Irizarry, M. C.; Hyman, B. T. Neurotoxic effects of thioflavin S-positive amyloid deposits in transgenic mice and Alzheimer's disease. *Proc. Natl. Acad. Sci. U.S.A.* **2002**, *99*, 13990−13995.
(30) Westermark, G. T.; Johnson, K. H.; Westermark, P. Staining methods for identification of amyloid in tissue. *Methods Enzymol.* **1999**, *309*, 3−25.
(31) Åslund, A.; Sigurdson, C. J.; Klingstedt, T.; Grathwohl, S.; Bolmont, T.; Dickstein, D. L.; Glimsdal, E.; Prokop, S.; Lindgren, M.; Konradsson, P.; Holtzman, D. M.; Hof, P. R.; Heppner, F. L.; Gandy, S.; Jucker, M.; Aguzzi, A.; Hammarström, P.; Nilsson, K. P. R. Novel pentameric thiophene derivatives for *in vitro* and *in vivo* optical imaging of a plethora of protein aggregates in cerebral amyloidoses. *ACS Chem. Biol.* **2009**, *4*, 673−684.
(32) Cook, N. P.; Torres, V.; Jain, D.; Martí, A. A. Sensing amyloid-β aggregation using luminescent dipyridophenazine ruthenium(II) complexes. *J. Am. Chem. Soc.* **2011**, *133*, 11121−11123.
(33) Hintersteiner, M.; Enz, A.; Frey, P.; Jaton, A.-L.; Kinzy, W.; Kneuer, R.; Neumann, U.; Rudin, M.; Staufenbiel, M.; Stoeckli, M.; Wiederhold, K.-H.; Gremlich, H.-U. *In vivo* detection of amyloid-β deposits by near-infrared imaging using an oxazine-derivative probe. *Nat. Biotechnol.* **2005**, *23*, 577−583.
(34) Klunk, W. E.; Bacskai, B. J.; Mathis, C. A.; Kajdasz, S. T.; McLellan, M. E.; Frosch, M. P.; Debnath, M. L.; Holt, D. P.; Wang, Y.; Hyman, B. T. Imaging Aβ plaques in living transgenic mice with multiphoton microscopy and methoxy-X04, a systemically administered Congo red derivative. *J. Neuropathol. Exp. Neurol.* **2002**, *61*, 797−805.
(35) Li, M.; Zhao, A.; Ren, J.; Qu, X. *N*-Methyl mesoporphyrin IX as an effective probe for monitoring Alzheimer's disease β-amyloid aggregation in living cells. *ACS Chem. Neurosci.* **2017**, *8*, 1299−1304.
(36) Liu, K.; Guo, T. L.; Chojnacki, J.; Lee, H.-G.; Wang, X.; Siedlak, S. L.; Rao, W.; Zhu, X.; Zhang, S. Bivalent ligand containing curcumin and cholesterol as a fluorescence probe for Aβ plaques in Alzheimer's disease. *ACS Chem. Neurosci.* **2012**, *3*, 141−146.
(37) Ono, M.; Ishikawa, M.; Kimura, H.; Hayashi, S.; Matsumura, K.; Watanabe, H.; Shimizu, Y.; Cheng, Y.; Cui, M.; Kawashima, H.; Saji, H. Development of dual functional SPECT/fluorescent probes for imaging cerebral β-amyloid plaques. *Bioorg. Med. Chem. Lett.* **2010**, *20*, 3885−3888.
(38) Ren, W.; Xu, M.; Liang, S. H.; Xiang, H.; Tang, L.; Zhang, M.; Ding, D.; Li, X.; Zhang, H.; Hu, Y. Discovery of a novel fluorescent probe for the sensitive detection of β-amyloid deposits. *Biosens. Bioelectron.* **2016**, *75*, 136−141.
(39) Cao, K.; Farahi, M.; Dakanali, M.; Chang, W. M.; Sigurdson, C. J.; Theodorakis, E. A.; Yang, J. Aminonaphthalene 2-cyanoacrylate (ANCA) probes fluorescently discriminate between amyloid-β and prion plaques in brain. *J. Am. Chem. Soc.* **2012**, *134*, 17338−17341.
(40) Cheng, Y.; Zhu, B.; Deng, Y.; Zhang, Z. In vivo detection of cerebral amyloid fibrils with smart dicynomethylene-4H-pyran-based fluorescence probe. *Anal. Chem.* **2015**, *87*, 4781−4787.
(41) Cui, M.; Ono, M.; Watanabe, H.; Kimura, H.; Liu, B.; Saji, H. Smart near-infrared fluorescence probes with donor-acceptor structure for in vivo detection of β-amyloid deposits. *J. Am. Chem. Soc.* **2014**, *136*, 3388−3394.
(42) Dao, P.; Ye, F.; Liu, Y.; Du, Z. Y.; Zhang, K.; Dong, C. Z.; Meunier, B.; Chen, H. Development of phenothiazine-based theranostic compounds that act both as inhibitors of β-amyloid aggregation and as imaging probes for amyloid plaques in Alzheimer's disease. *ACS Chem. Neurosci.* **2017**, *8*, 798−806.
(43) Fu, H.; Cui, M.; Tu, P.; Pan, Z.; Liu, B. Evaluation of molecules based on the electron donor-acceptor architecture as near-infrared β-amyloidal-targeting probes. *Chem. Commun.* **2014**, *50*, 11875−11878.
(44) Fu, H.; Cui, M.; Zhao, L.; Tu, P.; Zhou, K.; Dai, J.; Liu, B. Highly sensitive near-infrared fluorophores for in vivo detection of amyloid-β plaques in Alzheimer's disease. *J. Med. Chem.* **2015**, *58*, 6972−6983.
(45) Fu, H.; Tu, P.; Zhao, L.; Dai, J.; Liu, B.; Cui, M. Amyloid-β deposits target efficient near-infrared fluorescent probes: Synthesis, in vitro evaluation, and in vivo imaging. *Anal. Chem.* **2016**, *88*, 1944−1950.
(46) Kim, D.; Moon, H.; Baik, S. H.; Singha, S.; Jun, Y. W.; Wang, T.; Kim, K. H.; Park, B. S.; Jung, J.; Mook-Jung, I.; Ahn, K. H. Two-photon absorbing dyes with minimal autofluorescence in tissue imaging: Application to *in vivo* imaging of amyloid-β plaques with a negligible background signal. *J. Am. Chem. Soc.* **2015**, *137*, 6781−6789.
(47) Li, Q.; Lee, J.-S.; Ha, C.; Park, C. B.; Yang, G.; Gan, W. B.; Chang, Y.-T. Solid-phase synthesis of styryl dyes and their application as amyloid sensors. *Angew. Chem., Int. Ed.* **2004**, *43*, 6331−6335.
(48) Lv, G.; Cui, B.; Lan, H.; Wen, Y.; Sun, A.; Yi, T. Diarylethene based fluorescent switchable probes for the detection of amyloid-β pathology in Alzheimer's disease. *Chem. Commun.* **2015**, *51*, 125−128.
(49) Lv, G.; Sun, A.; Wei, P.; Zhang, N.; Lan, H.; Yi, T. A spiropyran-based fluorescent probe for the specific detection of β-amyloid peptide oligomers in Alzheimer's disease. *Chem. Commun.* **2016**, *52*, 8865−8868.

DOI: 10.1021/acsomega.8b00286
ACS Omega 2018, 3, 5141−5154

(50) Nesterov, E. E.; Skoch, J.; Hyman, B. T.; Klunk, W. E.; Bacskai, B. J.; Swager, T. M. *In vivo* optical imaging of amyloid aggregates in brain: Design of fluorescent markers. *Angew. Chem., Int. Ed.* **2005**, *44*, 5452−5456.
(51) Ono, M.; Watanabe, H.; Kimura, H.; Saji, H. BODIPY-based molecular probe for imaging of cerebral β-amyloid plaques. *ACS Chem. Neurosci.* **2012**, *3*, 319−324.
(52) Rajasekhar, K.; Narayanaswamy, N.; Murugan, N. A.; Kuang, G.; Ågren, H.; Govindaraju, T. A high affinity red fluorescence and colorimetric probe for amyloid β aggregates. *Sci. Rep.* **2016**, *6*, No. 23668.
(53) Ran, C.; Xu, X.; Raymond, S. B.; Ferrara, B. J.; Neal, K.; Bacskai, B. J.; Medarova, Z.; Moore, A. Design, synthesis, and testing of difluoroboron-derivatized curcumins as near-infrared probes for in vivo detection of amyloid-β deposits. *J. Am. Chem. Soc.* **2009**, *131*, 15257−15261.
(54) Sulatskaya, A. I.; Maskevich, A. A.; Kuznetsova, I. M.; Uversky, V. N.; Turoverov, K. K. Fluorescence quantum yield of thioflavin T in rigid isotropic solution and incorporated into the amyloid fibrils. *PLoS One* **2010**, *5*, No. e15385.
(55) Watanabe, H.; Ono, M.; Ariyoshi, T.; Katayanagi, R.; Saji, H. Novel benzothiazole derivatives as fluorescent probes for detection of β-amyloid and α-synuclein aggregates. *ACS Chem. Neurosci.* **2017**, *8*, 1656−1662.
(56) Watanabe, H.; Ono, M.; Matsumura, K.; Yoshimura, M.; Kimura, H.; Saji, H. Molecular imaging of β-amyloid plaques with near-infrared boron dipyrromethane (BODIPY)-based fluorescent probes. *Mol. Imaging* **2013**, *12*, 338−347.
(57) Watanabe, H.; Ono, M.; Saji, H. *In vivo* fluorescence imaging of β-amyloid plaques with push-pull dimethylaminothiophene derivatives. *Chem. Commun.* **2015**, *51*, 17124−17127.
(58) Yang, H.-Y.; Zhang, J.-J.; Zang, Y.; Zhang, H.-Y.; Li, J.; Chen, G.-R.; He, X.-P. D-A-D fluorogenic probe for the rapid imaging of amyloid β plaques *in vivo*. *Dyes Pigm.* **2017**, *136*, 224−228.
(59) Zhang, X.; Tian, Y.; Li, Z.; Tian, X.; Sun, H.; Liu, H.; Moore, A.; Ran, C. Design and synthesis of curcumin analogues for in vivo fluorescence imaging and inhibiting copper-induced cross-linking of amyloid beta species in Alzheimer's disease. *J. Am. Chem. Soc.* **2013**, *135*, 16397−16409.
(60) Zhou, K.; Fu, H.; Feng, L.; Cui, M.; Dai, J.; Liu, B. The synthesis and evaluation of near-infrared probes with barbituric acid acceptors for *in vivo* detection of amyloid plaques. *Chem. Commun.* **2015**, *51*, 11665−11668.
(61) Zhu, B.-y.; Cheng, Y.; Li, G.-b.; Yang, S.-y.; Zhang, Z.-r. Synthesis and evaluation of styrylpyran fluorophores for noninvasive detection of cerebral β-amyloid deposits. *Bioorg. Med. Chem.* **2016**, *24*, 827−834.
(62) Zhu, J.-y.; Zhou, L.-f.; Li, Y.-k.; Chen, S.-b.; Yan, J.-w.; Zhang, L. *In vivo* near-infrared fluorescence imaging of amyloid-β plaques with a dicyanoisophorone-based probe. *Anal. Chim. Acta* **2017**, *961*, 112−118.
(63) Rajasekhar, K.; Narayanaswamy, N.; Murugan, N. A.; Viccaro, K.; Lee, H.-G.; Shah, K.; Govindaraju, T. Aβ plaque-selective NIR fluorescence probe to differentiate Alzheimer's disease from tauopathies. *Biosens. Bioelectron.* **2017**, *98*, 54−61.
(64) Guan, Y.; Cao, K. J.; Cantlon, A.; Elbel, K.; Theodorakis, E. A.; Walsh, D. M.; Yang, J.; Shah, J. V. Real-time monitoring of Alzheimer's-related amyloid aggregation via probe enhancement-fluorescence correlation spectroscopy. *ACS Chem. Neurosci.* **2015**, *6*, 1503−1508.
(65) Heo, C. H.; Kim, K. H.; Kim, H. J.; Baik, S. H.; Song, H.; Kim, Y. S.; Lee, J.; Mook-jung, I.; Kim, H. M. A two-photon fluorescent probe for amyloid-β plaques in living mice. *Chem. Commun.* **2013**, *49*, 1303−1305.
(66) Heo, C. H.; Sarkar, A. R.; Baik, S. H.; Jung, T. S.; Kim, J. J.; Kang, H.; Mook-Jung, I.; Kim, H. M. A quadrupolar two-photon fluorescent probe for *in vivo* imaging of amyloid-β plaques. *Chem. Sci.* **2016**, *7*, 4600−4606.
(67) Li, Y.; Yang, J.; Liu, H.; Yang, J.; Du, L.; Feng, H.; Tian, Y.; Cao, J.; Ran, C. Tuning the stereo-hindrance of a curcumin scaffold for the selective imaging of the soluble forms of amyloid beta species. *Chem. Sci.* **2017**, *8*, 7710−7717.
(68) Li, Y.; Xu, D.; Sun, A.; Ho, S.-L.; Poon, C.-Y.; Chan, H.-N.; Ng, O. T. W.; Yung, K. K. L.; Yan, H.; Li, H.-W.; Wong, M. S. Fluoro-substituted cyanine for reliable *in vivo* labelling of amyloid-β oligomers and neuroprotection against amyloid-β induced toxicity. *Chem. Sci.* **2017**, *8*, 8279−8284.
(69) Mora, A. K.; Murudkar, S.; Alamelu, A.; Singh, P. K.; Chattopadhyay, S.; Nath, S. Benzothiazole-based neutral ratiometric fluorescence sensor for amyloid fibrils. *Chem. - Eur. J.* **2016**, *22*, 16505−16512.
(70) Jung, S.-J.; Park, S.-H.; Lee, E. J.; Park, J. H.; Kong, Y. B.; Rho, J. K.; Hur, M. G.; Yang, S. D.; Park, Y. D. Development of fluorescent probes that bind and stain amyloid plaques in Alzheimer's disease. *Arch. Pharm. Res.* **2015**, *38*, 1992−1998.
(71) Spano, F. C. The spectral signatures of Frenkel polarons in H- and J-aggregates. *Acc. Chem. Res.* **2010**, *43*, 429−439.
(72) Würthner, F.; Kaiser, T. E.; Saha-Möller, C. R. J-Aggregates: From serendipitous discovery to supramolecular engineering of functional dye materials. *Angew. Chem., Int. Ed.* **2011**, *50*, 3376−3410.
(73) Heinrich, G.; Schoof, S.; Gusten, H. 9,10-Diphenylanthracene as fluorescence quantum yield standard. *J. Photochem.* **1974**, *3*, 315−320.
(74) Derrick, J. S.; Lim, M. H. Tools of the trade: investigations into design strategies of small molecules to target components in Alzheimer's disease. *ChemBioChem* **2015**, *16*, 887−898.
(75) Kayed, R.; Head, E.; Sarsoza, F.; Saing, T.; Cotman, C. W.; Necula, M.; Margol, L.; Wu, J.; Breydo, L.; Thompson, J. L.; Rasool, S.; Gurlo, T.; Butler, P.; Glabe, C. G. Fibril specific, conformation dependent antibodies recognize a generic epitope common to amyloid fibrils and fibrillar oligomers that is absent in prefibrillar oligomers. *Mol. Neurodegener.* **2007**, *2*, No. 18.
(76) Kayed, R.; Head, E.; Thompson, J. L.; McIntire, T. M.; Milton, S. C.; Cotman, C. W.; Glabe, C. G. Common structure of soluble amyloid oligomers implies common mechanism of pathogenesis. *Science* **2003**, *300*, 486−489.
(77) Bitan, G.; Kirkitadze, M. D.; Lomakin, A.; Vollers, S. S.; Benedek, G. B.; Teplow, D. B. Amyloid β-protein (Aβ) assembly: Aβ40 and Aβ42 oligomerize through distinct pathways. *Proc. Natl. Acad. Sci. U.S.A.* **2003**, *100*, 330−335.
(78) Economou, N. J.; Giammona, M. J.; Do, T. D.; Zheng, X.; Teplow, D. B.; Buratto, S. K.; Bowers, M. T. Amyloid β-protein assembly and Alzheimer's disease: Dodecamers of Aβ42, but not of Aβ40, seed fibril formation. *J. Am. Chem. Soc.* **2016**, *138*, 1772−1775.
(79) Sitkiewicz, E.; Kłoniecki, M.; Poznański, J.; Bal, W.; Dadlez, M. Factors influencing compact-extended structure equilibrium in oligomers of Aβ1-40 peptide - An ion mobility mass spectrometry study. *J. Mol. Biol.* **2014**, *426*, 2871−2885.
(80) Fawzi, N. L.; Ying, J.; Ghirlando, R.; Torchia, D. A.; Clore, G. M. Atomic-resolution dynamics on the surface of amyloid-β protofibrils probed by solution NMR. *Nature* **2011**, *480*, 268−272.
(81) Spencer, R. K.; Li, H.; Nowick, J. S. X-ray crystallographic structures of trimers and higher-order oligomeric assemblies of a peptide derived from A$\beta_{17\text{-}36}$. *J. Am. Chem. Soc.* **2014**, *136*, 5595−5598.
(82) Cheon, M.; Chang, I.; Mohanty, S.; Luheshi, L. M.; Dobson, C. M.; Vendruscolo, M.; Favrin, G. Structural reorganisation and potential toxicity of oligomeric species formed during the assembly of amyloid fibrils. *PLoS Comput. Biol.* **2007**, *3*, 1727−1738.
(83) Beck, M. W.; Derrick, J. S.; Kerr, R. A.; Oh, S. B.; Cho, W. J.; Lee, S. J. C.; Ji, Y.; Han, J.; Tehrani, Z. A.; Suh, N.; Kim, S.; Larsen, S. D.; Kim, K. S.; Lee, J. Y.; Ruotolo, B. T.; Lim, M. H. Structural and mechanistic insights into development of chemical tools to control individual and inter-related pathological features in Alzheimer's disease. *Nat. Commun.* **2016**, *7*, No. 13115.
(84) Lee, H. J.; Korshavn, K. J.; Nam, Y.; Kang, J.; Paul, T. J.; Kerr, R. A.; Youn, I. S.; Ozbil, M.; Kim, K. S.; Ruotolo, B. T.; Prabhakar, R.; Ramamoorthy, A.; Lim, M. H. Structural and mechanistic insights into development of chemical tools to control individual and inter-related pathological features in Alzheimer's disease. *Chem. - Eur. J.* **2017**, *23*, 2706−2715.
(85) Derrick, J. S.; Kerr, R. A.; Nam, Y.; Oh, S. B.; Lee, H. J.; Earnest, K. G.; Suh, N.; Peck, K. L.; Ozbil, M.; Korshavn, K. J.; Ramamoorthy, A.;

DOI: 10.1021/acsomega.8b00286
ACS Omega 2018, 3, 5141−5154

Prabhakar, R.; Merino, E. J.; Shearer, J.; Lee, J.-Y.; Ruotolo, B. T.; Lim, M. H. A redox-active, compact molecule for cross-linking amyloidogenic peptides into nontoxic, off-pathway aggregates: in vitro and in vivo efficacy and molecular mechanisms. *J. Am. Chem. Soc.* **2015**, *137*, 14785−14797.

(86) Derrick, J. S.; Kerr, R. A.; Korshavn, K. J.; McLane, M. J.; Kang, J.; Nam, E.; Ramamoorthy, A.; Ruotolo, B. T.; Lim, M. H. Importance of the dimethylamino functionality on a multifunctional framework for regulating metals, amyloid-β and oxidative stress in Alzheimer's disease. *Inorg. Chem.* **2016**, *55*, 5000−5013.

(87) Derrick, J. S.; Lee, J.; Lee, S. J. C.; Kim, Y.; Nam, E.; Tak, H.; Kang, J.; Lee, M.; Kim, S. H.; Park, K.; Cho, J.; Lim, M. H. Mechanistic insights into tunable metal-mediated hydrolysis of Amyloid-β peptides. *J. Am. Chem. Soc.* **2017**, *139*, 2234−2244.

(88) Mruk, D. D.; Cheng, C. Y. Enhanced chemiluminescence (ECL) for routine immunoblotting: An inexpensive alternative to commercially available kits. *Spermatogenesis* **2011**, *1*, 121−122.

DOI: 10.1021/acsomega.8b00286
ACS Omega 2018, 3, 5141−5154